Hydrogeochemical and isotopic signatures elucidate deep subsurface hypersaline brine formation through radiolysis driven water-rock interaction

D.M. Nisson [a,*], T.L. Kieft [b], H. Drake [c], O. Warr [d,e], B. Sherwood Lollar [d,f], H. Ogasawara [g], S.M. Perl [h], B.M. Friefeld [i], J. Castillo [j], M.J. Whitehouse [k], E. Kooijman [k], T.C. Onstott [a]

[a] Department of Geosciences, Princeton University, Princeton, NJ 08540, USA
[b] Biology Department, New Mexico Institute of Mining and Technology, Socorro, NM 87801, USA
[c] Department of Biology and Environmental Science, Linnaeus University, 391 82 Kalmar, Sweden
[d] Department of Earth Sciences, University of Toronto, Toronto, Ontario M5S 3B1, Canada
[e] Department of Earth Sciences, University of Ottawa, Ottawa, Ontario K1N 6N5, Canada
[f] Institut de Physique du Globe de Paris (IPGP), Université Paris Cité, France
[g] College of Science and Engineering, Ritsumeikan University, Kusatsu, Shiga 525-8577, Japan
[h] Jet Propulsion Laboratory, Pasadena, CA 91109, USA
[i] Lawrence Berkeley National Laboratory, Berkeley, CA 94720, USA
[j] Department of Microbiology and Biochemistry, University of the Free State, Bloemfontein 9300, South Africa
[k] Swedish Museum of Natural History, 104 05 Stockholm, Sweden

ARTICLE INFO

ABSTRACT

Geochemical and isotopic fluid signatures from a 2.9–3.2 km deep, 45–55 °C temperature, hypersaline brine from Moab Khotsong gold and uranium mine in the Witwatersrand Basin of South Africa were combined with radiolytic and water–rock isotopic exchange models to delineate brine evolution over geologic time, and to explore brine conditions for habitability. The Moab Khotsong brines were hypersaline (Ca-Na-Cl) with 215–246 g/L TDS, and Cl^- concentrations up to 4 mol/L suggesting their position as a hypersaline end-member significantly more saline than any previously sampled Witwatersrand Basin fluids. The brines revealed low DIC ($\sim$0.266–$\sim$1.07 mmol/L) with high ($\sim$8.49–$\sim$23.6 mmol/L) DOC pools, and several reduced gaseous species (up to 46 % by volume H_2) despite microoxic conditions (Eh = 135–161 mV). Alpha particle radiolysis of water to H_2, H_2O_2, and O_2 along with anhydrous-silicate-to-clay alteration reactions predicted 4 mol/L Cl^- brine concentration and deuterium enrichment in the fracture waters over a period > 1.00 Ga, consistent with previously reported ^{40}Ar noble gas-derived residence times of 1.20 Ga for this system. In addition, radiolytic production of 7–26 nmol/(L × yr) H_2, 3–11 nmol/(L × yr) O_2, and 1–8 nmol/(L × yr) H_2O_2 was predicted for 1–100µ g/g ^{238}U dosage scenarios, supporting radiolysis as a significant source of H_2 and oxidant species to deep brines over time that are available to a low biomass system (10^2–10^3 cells/mL). The host rock lithology was predominately Archaean quartzite, with minerals exposed on fracture surfaces that included calcite, pyrite, and chlorite. Signatures of $\delta^{18}O_{calcite}$, $\delta^{13}C_{calcite}$, $\Delta^{33}S_{pyrite}$, $\delta^{34}S_{pyrite}$ and $^{87}Sr/^{86}Sr$ obtained from secondary ion mass spectrometry (SIMS) microanalyses suggest several discrete fluid events as the basin cooled from peak greenschist conditions to equilibrium with present-day brine temperatures. The brine physiochemistry, geochemistry, and cellular abundances were significantly different from those of a younger, shallower, low salinity dolomitic fluid in the same mine, and both were different from the mine service water. These results indicate the discovery of one of few long-isolated systems that supports subsurface brine formation via extended water–rock interaction, and an example of a subsurface brine system where abiotic geochemistry may support a low biomass microbial community.

* Corresponding author.
E-mail address: dnisson@princeton.edu (D.M. Nisson).

1. Introduction

The deep terrestrial subsurface globally represents a network of dynamic geochemical environments, principally fracture waters housed within deep crystalline and paleo-sedimentary rocks (Onstott et al., 2006; Kietäväinen et al., 2013; Frape et al., 2014; Sherwood Lollar et al., 2014; Magnabosco et al., 2016; Drake et al., 2021; Warr et al., 2021). Depending on the extent of their hydrogeologic isolation, these deep fluid environments can harbor oligotrophic conditions, large quantities of reduced gas species (e.g. H_2 and CH_4), and sub-neutral pH (Ward et al., 2004; Onstott et al., 2006; Sherwood Lollar et al., 2006; Frape et al., 2014; Simkus et al., 2016). In these low porosity rock environments, fluids can also reach high salinities at depth, in some cases harboring hypersaline brines (Carpenter, 1978; Vovk, 1981, 1982, 1987; Fritz and Frape, 1982; Frape et al., 1984; Gascoyne et al., 1989; Bottomley et al., 1994; Kloppmann et al., 2002; Kharaka and Hanor, 2003; Onstott et al., 2006; Shouakar-Stash et al., 2007; Li et al., 2016; Magnabosco et al., 2018; Warr et al., 2021). Subsurface continental brines have been studied extensively in terms of the origin of their salinity and their geochemical relationship with *in situ* microbial processes. There is greater literature representation, however, of shallower brine systems that experience shorter periods of hydrologic isolation (typically formed over months to thousands of years) that can support higher biomass systems due to more recent (or current) infiltration of surface-derived fluids (Table S1). There are few examples, however, considering deep (>2 km) continental brines that reveal long periods of hydrologic isolation, with residence times on million to even billion-year timescales (Table S1). Those with accompanying microbial characterization have been previously identified in the Szczecin Trough of Stargard, Poland, the KTB deep borehole in Germany, the Precambrian crystalline basements of the Witwatersrand Basin of South Africa, and the Fennoscandian and Canadian Shields (Table S1) (Kietäväinen et al., 2013; Warr et al., 2018, 2021; Lollar et al., 2019; Kalwasińska et al., 2020).

While the fluids at these locations reflect different proposed formation mechanisms, they are all the product of water–rock interaction occurring over long time periods in hydrogeologic isolation. Examples of such processes include: evaporitic dissolution and magmatic HCl interaction (>2.58 Ma, Stargard, Poland) (Kalwasińska et al., 2020), silicate hydration (20–50 Ma, Outokumpu, Finland) (Kietäväinen et al., 2013, 2014), as well as serpentinization and water radiolysis (>1.00 Ga, Kidd Creek, Canada) (Frape et al., 1984; Warr et al., 2021). Formation of saline deep fluids in the deep boreholes of Germany, Sweden, and Kloof Mine of South Africa's Witwatersrand Basin, have a less certain history, with subsurface geochemical trends suggesting their salinity may have been acquired through some type of water–rock interactions under largely isolated conditions or mixing with higher salinity fluids over time (Gold, 1992; Möller et al., 1997; Onstott et al., 2006; Kieft et al., 2018). Despite their differing formation mechanisms, these deep brine systems primarily support low biomass ($\sim$10^3–10^4 cells/mL) and low diversity communities, with dominance of anaerobic chemolithotrophic metabolic strategies including sulfate/nitrate reduction and various forms of methanogenesis (Table S1). With so few examples of naturally formed deep brines, and even fewer sites capable of supporting *in situ* communities in hydrogeochemical isolation, more studies of these systems are important to understand how brine geochemical history influences conditions for habitability. To address the lack of characterization for deep continental subsurface brines in the literature, this study provides a new opportunity to investigate how brine formation history influences conditions for microbial habitability in deep subsurface systems, by considering the current geochemistry alongside the salinity and isotopic evolution of a hypersaline (215–246 g/L), long-isolated (1.20 Ga) brine at 2.9–3.2 km depth in Moab Khotsong gold and uranium mine located in the Witwatersrand Basin of South Africa.

The presence of a high radiogenic contribution from ^{238}U in the host rock of Moab Khotsong (supported by the first ever radiogenic ^{86}Kr excess detected in free fluids (Warr et al., 2022)) allows us to consider radiolysis as a potentially dominant water–rock process in deep brine salinity evolution and habitability. Radiolysis has been found to produce H_2, in addition to oxidant species (H_2O_2 and O_2) for use by chemolithotrophs, with rates of radiolytic production that increase with increasing fluid chloride concentrations (Lin et al., 2005b; Buck et al., 2012). Radiolytically-produced oxidant species can react with host rock, producing additional electron donor/acceptor species, including sulfate (SO_4^{2-}) and nitrite/nitrate (NO_2^-/NO_3^-) where sulfide minerals (Lefticariu et al., 2010; Dos Santos et al., 2016; Li et al., 2016) or ammonia (Silver et al., 2012), respectively, are present. If there are not enough radiolytic products remaining for the regeneration of H_2O, then this process could potentially lead to brine formation (Warr et al., 2021), in addition to a self-sustaining abiogenic redox environment and carbon pool if the system has been isolated over long timescales under conditions of low porosity/permeability (Sherwood Lollar et al., 2014, 2021).

Other water–rock interactions that can alter the geochemical/isotopic evolution of subsurface brines, and potentially at Moab Khotsong, include the formation of secondary clay minerals from the hydration of mafic and ultramafic species (Charlou et al., 2002; Etiope and Sherwood Lollar, 2013; Schrenk et al., 2013; Sherwood Lollar et al., 2014). Depending on the species of clay formed, water can be held in the silicate interlayer structure as well as adsorbed to surface sites, removing it from the larger fluid system (Barton and Karathanasis, 2002; Kloppmann et al., 2002; Ehlmann et al., 2011), and in some continental subsurface settings, this process can produce significant quantities of H_2 ($\sim$10^10–10^11 mol/yr) (Sherwood Lollar et al., 2014; Worman et al., 2016) with these processes contributing to shifts in fluid δ^2H signature (Kloppmann et al., 2002; Warr et al., 2021). Just as the degree of radiolysis depends on the concentration of local radionuclides like ^{238}U, however, the degree of contribution by silicate hydration to H_2O loss, H_2 production, and fluid δ^2H evolution largely depends on the lithology at each specific site. Additionally, stable isotopic micro-analyses of fracture-coating minerals including $\Delta^{33}S$ and $\delta^{34}S$ of pyrite, $\delta^{13}C$ of calcites and $\delta^{18}O$ of calcites/quartz, in addition to $^{87}Sr/^{86}Sr$ signatures have been used along with radioisotopic dating in less saline subsurface systems to constrain fluid recharge events, microbial activity, heating and cooling episodes, and relative timing of equilibrium between the fluid chemistry with host rock species (Blyth et al., 2000, 2004,2009; Stotler et al., 2009; Li et al., 2016; Drake et al., 2015, 2021). Combined with noble gas residence times capable of quantifying the Ma–Ga timescales these global systems can operate over (Lippmann-Pipke et al., 2003, 2011; Holland et al., 2013; Kietäväinen et al., 2014; Heard et al 2018; Warr et al., 2018), a thorough analysis of the surrounding lithology could be applied to deep subsurface brines to determine the contribution of water–rock processes in shaping brine formation, to constrain precursor fluid infiltration and/or recharge, and to understand if habitable conditions are present.

In this study we investigate the contributions of water–rock interactions over time to the timing and formation of salinity and isotopic signatures in the Moab Khotsong brine over its > 1.00 Ga residence time, and to the potential for microbial habitability in isolation. We start by characterizing the current geochemistry, and biomass of the Moab Khotsong brines. With prior knowledge of high radiolytic activity in the Moab system (Warr et al., 2022),

we employ a model of alpha-particle driven radiolysis to evaluate the role of this water–rock process as a primary driver of salinity evolution in the brines, and δ^2H_{Brine} evolution, alongside processes of silicate hydration. We then explore isotopic evolution of the surrounding lithology, including constraints on the timing and type of precursor fluid flow events, through signatures of fracture lining minerals including $\Delta^{33}S$ and $\delta^{34}S$, $\delta^{13}C$, $\delta^{18}O$, and $^{87}Sr/^{86}Sr$. Finally, we consider the rates of redox/carbon contributions from dominant water–rock processes in the system, coupled to estimates of current biomass, to see if the current brines allow for a self-sustaining, habitable environment. This work contributes to our understanding of how brine geochemical history influences conditions for habitability by characterizing a highly radiogenic, deep continental subsurface brine system that is one of two globally with a residence time > 1.00 Ga.

2. Materials and methods

2.1. Site characteristics and thermal history

Moab Khotsong gold mine is situated in the 2.10–3.00 Ga Witwatersrand Basin, in the southernmost zone of the Klerksdorp gold mining region in South Africa (Fig. 1a). The basin is composed of the 2.20–2.50 Ga Transvaal Supergroup (dolomite, banded iron formation), the 2.70 Ga Ventersdorp Supergroup (siltstone, quartzite, and metavolcanics), and the 2.90 Ga Witwatersrand Supergroup (metavolcanics, quartzite, and shale) (Tucker et al., 2016; Kieft et al., 2018). The major gold bearing reef that is actively mined in the Klerksdorp region is the Vaal Reef (Pienaar et al., 2015), and it represents a site of high gold, uranium, and organic carbon concentrations as a likely consequence of their co-deposition (Gray et al. 1998; Fuchs et al., 2017; Frimmel, 2019). This study included fluid, microbiological, and core samples collected from three different depths in Moab Khotsong mine: the 1200 level (1.2 kmbls) intersecting the Transvaal Supergroup dolomites, and the 95 (2.9 kmbls) and 101 (3.1 kmbls) levels intersecting quartzites of the West Rand Group within the Witwatersrand Supergroup (Fig. 1b). The brines at 95 and 101 levels occur in mineralized fractures in contact with dolerite sills and surrounding quartzites (Fig. S1). The 1200 level samples come from a regional karstic aquifer hosted by dolomites belonging to the Malmani Subgroup of the Chuniespoort Group (Catuneanu and Biddulph, 2001) and represents a control system for evaluating surface redox/carbon contribution due to potential fluid mixing or contamination in the brines.

The Witwatersrand Basin history is marked by numerous metamorphic events, serving as potential windows for fluid circulation and metamorphism throughout the stratigraphy. Most relevant to this study include catastrophic metamorphism and hydrothermal fluid circulation during the Vredefort meteorite impact at 2.02 Ga (Frimmel, 2005), during the deposition of the Pretoria Group at 2.10–2.20 Ga (where regional peak greenschist facies temperatures of 300–350 °C were reached in the basin) (Frimmel, 2005; Frimmel, 2019), and more recently, during the potential uplift of the South African plateau (~90–70 Ma) which affected the top 1–2 km of sediment across the plateau (Braun et al., 2014).

2.2. Sampling of deep fracture waters

Fracture waters on each of the three levels (1200, 95, and 101) were sampled from one borehole previously drilled by the mine on that level and were flushed for at least four minutes prior to sample collection. Samples from the 1200 and 101 levels were collected with a sterile, stainless-steel multi-valve manifold (Lau et al., 2014). On the 1200 level, this manifold is attached to a rubber hose extending from the dam of the main pump station on that level, with a continuous flow of ~15 L/min at all times, ensuring continuous flushing of the hose even in the absence of active sampling. On the 101 level, this manifold is connected directly to steel borehole casing (−5° inclination). This borehole is sealed in the absence of sampling with a stainless-steel valve, allowing fluid buildup under pressure; fluid begins to flow from the borehole at the onset of sampling when this valve is replaced with the manifold, allowing for controlled flow (~100 mL/min) during sample collection.

The 95 level borehole was drilled at a −47° inclination and yielded 800 m of core from the West Rand Group. A U-tube and packer system (Freifeld et al., 2005; Freifeld, 2009) isolated the 95 level borehole just above the fracture zone and allowed for brine outflow to be controlled (~112 mL/min) through Inconel tubing that was flushed with N_2 and sealed following each sampling. This U-tube and packer system was also equipped with a downhole pressure and temperature sensor to continuously monitor in situ physiochemical parameters (Fig. S2). Finally, a collection of service water used by the mine for general drilling and cleaning purposes was taken from an outlet on the 95 level portion of the service water pipeline. This served as a control for any contamination
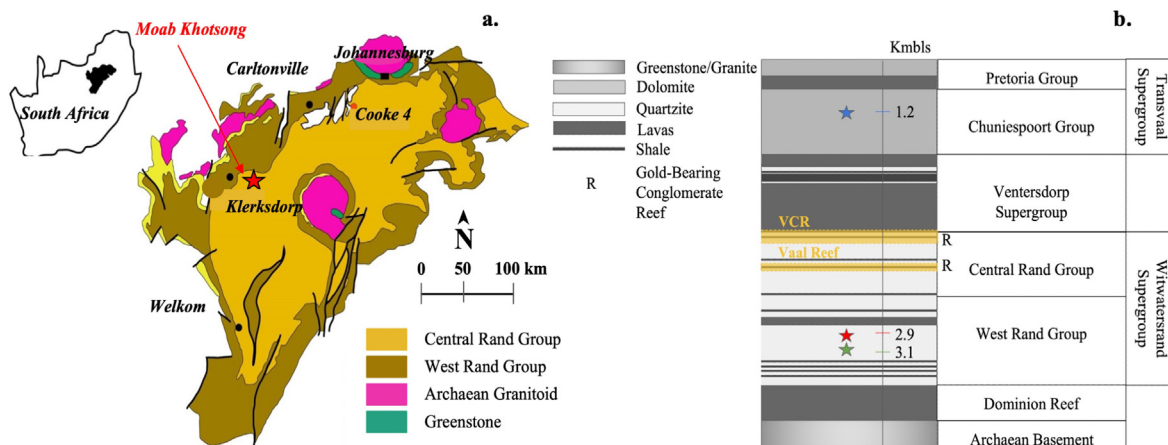

Fig. 1. (a) Geological map of Witwatersrand Basin and location of Moab Khotsong mine (modified from Mngadi et al. (2019)) and (b) the Witwatersrand Basin lithological column, including major reef locations [Ventersdorp Contact Reef (VCR)] and borehole access depths at Moab Khotsong mine (blue star – 1200 level, red star – 95 level and green star – 101 level). (For interpretation of the references to colour in this figure legend, the reader is referred to the web version of this article.)

introduced through drilling of the borehole, which used service water as the drilling fluid. Distribution of service water throughout the mine follows a continuous water reticulation pipeline through a surface cooling refrigeration system and down through various subsurface dams (Vosloo, 2008). A barium-based drilling grease (AMC GORILLA GRIP™), drilling lubricant (AMC EZYCORE™), degreasing fluid (AMC TRIPLE 4™), and fluorescein dye were used in the drilling process of each borehole, but due to several years having passed since drilling, we do not expect them to play any significant role in the geochemical characterization of the fluids.

Nalgene bottles used for the collection of various fluid samples were washed in a 10 % HCl bath overnight prior to sampling. Filtered water was collected in 15 mL polypropylene Falcon tubes for anion analysis and with the addition of 1 mL HNO_3 for cation analysis. One-liter amber bottles used for collection of dissolved organic carbon (DOC) and dissolved inorganic carbon (DIC) analysis on filtered water were similarly acid-washed and then combusted overnight at 450 °C (Simkus et al., 2016; Kieft et al., 2018). DIC samples were poisoned with 0.5 µL/ml of saturated $HgCl_2$, and gently filled to the top with all visible air bubbles removed prior to sealing. DOC samples were filled 3/4 full and frozen. All filtered water samples were collected using a 0.2µ m pore size as these same filters were saved for future nucleic acid extractions. A gas stripper device was connected to the manifold or U-tube for collection of dissolved gas samples. The gas was collected in 160 mL vacuum-evacuated serum vials following the methods of Ward et al. (2004).

2.3. Geochemical and isotopic signatures of fracture waters

Measurements of pH, salinity, temperature, and oxidation–reduction potential (ORP) were taken on site with pre-calibrated Hanna BioSolutions handheld probes (Hanna Instruments, Woonsocket, RI, USA), excluding the 95 level in which a downhole temperature sensor was used. To calculate Eh, field measured ORP was corrected for temperature against an $Ag/AgCl_2$ reference. Measurements of dissolved oxygen, hydrogen sulfide, and total iron were made on site using CHEMetrics colorimetric test kits (CHEMetrics, Midland, VA, USA), and the maximum measurement taken in the field was reported for these species. Anions and low molecular weight organic acids were measured using a Dionex ICS-5000 ion chromatograph (Dionex Corp., Sunnyvale, CA, USA) in the Onstott Lab at Princeton University. Correlation significance between anions Cl^- and Br^- for Witwatersrand Basin samples was determined with the "t-Test: Paired Two Sample for Means" package in Excel, using a significance threshold of α = 0.05 (two-tailed p-value reported). Cations were quantified by inductively coupled plasma mass spectrometry at Activation Laboratories Ltd. (ISO/IEC 17025 certified) in Ontario, Canada. Samples designated for NH_4^+ were acidified in the field with the addition of 200 µL conc. H_2SO_4 (50 %) prior to filtered water collection in 60 mL serum vials. NH_4^+ was then quantified from these samples in the Onstott Lab using the sodium nitroprusside-phenol colorimetric method (Strickland and Parsons, 1972). Charge balance was confirmed for ions using Geochemist's Workbench V.14 (Bethke et al., 2020). Total dissolved solids (TDS) was taken to be the sum of all cations, anions, and proportion of DIC precipitated as bicarbonate (DIC*0.4917) in each sample. Gas compositions of Ar, and hydrocarbons (CH_4, C_2H_6 and C_3H_8) were determined in the Stable Isotope Laboratory at the University of Toronto on a Varian 3800 GC (µTCD) and a Varian 3400 GC (FID) respectively, both using a He carrier gas. All other gas compositions were determined at the Onstott Lab with coupled TCD, RCP, and FID units (Peak Laboratories, Mountain View, CA, USA), and using an Ar carrier gas. Gas measurements for the brine samples were corrected for air contamination by assuming all O_2 was from air and calculating the

corresponding N_2 composition from an air N_2/O_2 ratio (3.76) and Ar composition from an Ar/O_2 ratio (0.0446). Stable water isotopes $\delta^{18}O$ and δ^2H were determined by the Environmental Isotope Laboratory at the University of Waterloo (after the methods described in Ward et al. (2004) and Warr et al. (2021). Oxygen isotope ratios and hydrogen isotope ratios for water samples were measured to a precision of ±0.2 ‰ and ±0.8 ‰, respectively.

Measurements of fluid $^{87}Sr/^{86}Sr$ were performed in the Onstott and Schoene Labs at Princeton University. Sr quantities of 300–500 ng from each fluid sample were fully dried in uncapped Teflon beakers at 220 °C and then redissolved in 500 µL of 3.5 eq/L HNO_3. Sr was separated and purified from each fluid sample using Teflon microcolumns containing Sr-spec cation exchange resin as per the methods of Lundblad (1994). This involved pre-washing resin columns with 3 eq/L HCl, followed by MQ H_2O rinse (x3). Samples were drained through columns, followed by a MQ H_2O rinse. Then, 500 µL of 3.5 N HNO_3 was allowed to filter through, followed by the addition of 1 drop 3.5 eq/L HNO_3 (x3) and 300 µL of 3.5 eq/L HNO_3 (x4), respectively. Samples were eluted to 300–500 µL final volume with MQ H_2O. $^{87}Sr/^{86}Sr$ ratios were measured by loading half the sample onto Re-ribbon filaments with TaF_5 and analyzed two to three times each using a IsotopX PhoeniX62 thermal ionization mass spectrometer. $^{87}Sr/^{86}Sr$ data were normalized relative to the reference material SM 987 with an accepted value of 0.710248 (McArthur et al., 2006)). Replicate analysis of standard reference material (SRM) 987 ranged from 0.71 $\pm$ 1.56261E-05 (2σ, n = 285) to 0.710249 $\pm$ 9.23E-06 (2σ, n = 284).

DOC and DIC were measured using a 1030 W TOC Analyzer (OI Analytical, College Station, Texas, USA) in the Onstott Lab using an adapted protocol to the one outlined in Simkus et al. (2016); further detail on optimization for high chlorinity samples is included in Supplementary Material. The δ^{13}C-CO_2 compositions were measured using a Picarro G2101-i Isotopic CO_2 Cavity Ring Down Spectrometer (CRDS) (Picarro Inc., Santa Clara, CA, USA) with a precision of ±0.3 ‰ for DIC and DOC. These measurements were made on CO_2 passed directly from the Aurora 1030 W to a Picarro Caddy Continuous Flow Interface (A2100) following quantification of DOC or DIC. Picarro CRDS measurements of δ^{13}C for both DIC and DOC were corrected against an intra-laboratory δ^{13}C standard expressed with respect to V-PDB and its measured value on the CRDS, following equation (3) in Chen et al. (2013). Detection limits and error for all geochemical measurements are included in Table S2 of Supplementary Material, except for isotopic measurements for core samples and $^{87}Sr/^{86}Sr$ for the brines, which are included in their respective supplementary data files.

2.4. Geochemical and isotopic signatures of host rock

Measurements of $^{87}Sr/^{86}Sr$ for identified calcite (n = 52) were collected via LA-MC-ICP-MS analysis at the Vegacenter of the Swedish Museum of Natural History, in Stockholm, Sweden, using a Nu plasma (II) MC-ICP-MS and ESI NWR193 ArFeximer laser ablation (15 Hz) system following methods presented in Drake et al. (2021). The spot size was 80 µm, fluence 2.7 J/cm^2, with washout and ablation times of 40 and 45 s, respectively. All measurements for $^{87}Sr/^{86}Sr$ were normalized to an in-house brachiopod reference material "Ecnomiosa gerda" (linear drift and accuracy correction) using a value established by TIMS of 0.709168 (2sd 0.000004) (Kiel et al., 2014). A modern oyster shell from Western Australia was used as a secondary reference material and was analyzed at regular intervals along with the primary reference. Comparison to the modern seawater value for $^{87}Sr/^{86}Sr$ of 0.7091792 $\pm$ 0.0000 021 (Mokadem et al., 2015) was used to quantify the accuracy of these analyses. Reference standard values are included in supplementary data.

SIMS measurements were performed at the Swedish Museum of Natural History, Stockholm (NordSIMS facility) for $\delta^{13}C$ and $\delta^{18}O$ in identified calcite veins and for multiple sulfur isotopes ($\delta^{33}S_{VCDT}$, $\delta^{34}S_{VCDT}$, and $\Delta^{33}S$ (=$\delta^{33}S - 1000$ (($1 + \delta^{34}S/1000$) 0.515–1)) of identified pyrite. These analyses were made using a CAMECA IMS1280 ion microprobe applying 10 μm spot size and 1–2 μm depth dimensions. Instrument settings for sulfur isotopes are detailed in Whitehouse (2013) and Drake et al. (2013). Sulfur was sputtered using a $^{133}Cs +$ primary beam with 20 kV incident energy (10 kV primary, −10 kV secondary) and a primary beam current of ~1.5nA. A normal incidence electron gun was used for charge compensation. Analyses were performed in automated sequences, with each analysis comprising a 70 s pre-sputter to remove the gold coating over a rastered 15 × 15 μm area, centering of the secondary beam in the field aperture to correct for small variations in surface relief, and data acquisition in 16 four-second integration cycles. The magnetic field was locked at the beginning of the session using a nuclear magnetic resonance (NMR) field sensor. Secondary ion signals for ^{33}S and ^{34}S were detected simultaneously using Faraday detectors with a common mass resolution of 4860 (M/ΔM). Data were normalized for instrumental mass fractionation using matrix matched reference materials which were mounted together with the sample mounts. For multiple sulfur isotopes, non-MIF Ruttan pyrite (n = 38) and Balmat pyrite (n = 18) were used as standards following Crowe and Vaughan (1966) with values redetermined by Cabral et al. (2013). Ruttan pyrite was used as the primary $\delta^{34}S$ reference ($\delta^{34}S = 1.41$ ‰ ± 0.05 ‰ SD), while both were used to define the mass dependent fractionation line ($\Delta^{33}S$ ± 0.14 ‰ SD for both standards). Additional pyrite references used included S0302A (n = 13), with $\delta^{34}S = 0.00 ± 0.07$ ‰ SD and $\Delta^{33}S = −0.050 ± 0.13$ ‰ SD, and Isua(Is)–5A MIF pyrite (n = 7), with $\delta^{34}S = 2.60 ± 0.10$ ‰ SD and $\Delta^{33}S = 2.53 ± 0.13$ ‰ SD. The higher dispersion in $\Delta^{33}S$ for Isua(Is)–5A relative to other grains from this material suggested some MIF heterogeneity, but within the error of the value reported by Whitehouse (2013). Reference standard values for SIMS analyses are included in supplementary data.

Measurements of $\delta^{13}C$ and $\delta^{18}O$ in calcite follow those described for S isotopes, with some differences. Two Faraday cups and a mass resolution 2500 were used for measurements of O. A combination of a Faraday cup and electron multiplier was used for measurements of C, along with a mass resolution of 2500 on the ^{12}C peak and of 4000 on the ^{13}C peak to resolve it from $^{12}C^1H$, following settings in Drake et al. (2015, 2021). Isotope data from calcite were normalized using calcite reference material S0161 from a granulite facies marble in the Adirondack Mountains, kindly provided by R.A. Stern (Univ. of Alberta). The values used for instrumental mass fractionation correction were determined by conventional stable isotope mass spectrometry at Stockholm University on ten separate pieces, yielding $\delta^{13}C = 0.22$ ‰ ± 0.35 ‰$_{-VPDB}$ (1 std. dev.) and $\delta^{18}O = -5.62$ ‰ ± 0.22 ‰$_{-VPDB}$ (1 std. dev.).

2.5. Fluorescent cell imaging and counts

Water samples for cell counts were collected on-site in 50 mL Falcon polystyrene tubes containing 5 mL of filter (0.2 μm) sterilized 37 % formaldehyde and stored at 4 °C (Kovacik, 2002; Kyle et al., 2008). Cells were concentrated and stained with SYTO-9 DNA green fluorescent dye per the methods of Liang et al. (2019) (further detail described in Supplementary Material). Cells from the 1200 level were enumerated (n = 3) taking the average of 30 fields of view using epifluorescent microscopy at 1000× magnification. Cell concentrations in the 95 and 101 level brine samples were too low to be consistently observed under epiflourescent microscopy, and instead were measured under Raman microscopy (viewing window of 60 μm × 120 μm with 50x objective). All

organisms exhibiting non-Brownian motion within a 5 μL aliquot of each sample (n = 5 for 95 level, n = 3 for 101 level) were counted and validated as microbial cells.

2.6. Modeling the impacts of radiolysis + silicate hydration on brine salinity formation

Due to the long subsurface residence time of the Moab Khotsong brines (as supported by ^{40}Ar noble gas-derived residence times > 1.00 Ga presented in Warr et al. (2022) for this system) extensive water–rock interactions were investigated as a way to produce high salinities in subsurface fracture fluids. Specifically, here we propose a new numerical model to investigate and quantify the role and rates of radiolysis in brine formation which was previously considered by Vovk et al (1981; 1987). Given the high uranium concentrations reported in the ore zones of the Witwatersrand Basin, a range of 1–100 μg/g ^{238}U was considered for alpha-particle driven, radiolytic formation of 4 mol/L Cl^- brine from less saline precursor fluids, with the lower bound represented by average U concentrations from borehole host rock core sections (Table S3). The upper bound was estimated from Beatrix gold mine fracture water based upon its $^{36}Cl/Cl × 10^{-15}$ value, and a ^{238}U of host rock vs $^{36}Cl/Cl × 10^{-15}$ of fracture fluid correlation reported by Purtschert et al. (2021). This range includes a 20 μg/g U host rock concentration estimated from ^{40}Ar and ^{136}Xe noble gas ages for this brine by Warr et al. (2022) as well as the < 11 μg/g derived as the maximum correlative estimate using the $^{36}Cl/Cl × 10^{-15}$ ratio obtained in this study (Table S4). To see if radiolysis via ^{238}U decay could have significantly contributed to brine concentration, radiolytic splitting of H_2O into H_2 and oxidants H_2O_2 (primary) and O_2 (secondary) was modeled over geologic time with the evolution of the fluid from a Precambrian seawater precursor (1 mol/L Cl^-) (De Ronde et al., 1997) or a less saline hydrothermal precursor (0.5 mol/L Cl^-) (Grové and Harris, 2010) to the current day 4 mol/L Cl^-.

In this study, primary species yields for 1–4 mol/L Cl^- were obtained from a linear interpolation of primary yields for 0 mol/L Cl^- and 5 mol/L Cl^- solutions from Kelm and Bohnert (2004), assuming alpha radiolysis as the primary form of radiolytic decay from U (Table S5). To determine primary reaction rates at each chlorinity, the primary yield for H_2 (G^0_{H2}) was converted from number of species formed per 100 eV to mol/L × Gy. This value was then multiplied by the dosage rate of 0.389 Gy/sec used for alpha radiolytic experiments in Kelm and Bohnert (2004) to obtain the molar concentration of H_2 that should be produced after 1 s of reaction. The reaction rate of the primary reaction was then modified until the correct molar concentration of H_2 was produced following a 1 s reaction run in the program Kintecus (Ianni, 2003), with all secondary reactions turned off. Further background regarding the process of radiolysis in subsurface brine systems and the background of the model employed in this study is included in Supplementary Material. Primary reactions were run in addition to secondary reactions from Bjergbakke et al. (1989) and Kelm and Bohnert (2004) using Kintecus (Table S6). Secondary reactions were run under increasing concentrations of Cl^-, Br^-, SO_4^{2-}, HCO_3^-, CH_4, and Fe^{2+} linearly extrapolated from freshwater to values of the current 95 level brine, to obtain secondary yields for H_2, H_2O_2, O_2, and H_2O in number of species formed per 100 eV. Secondary yields were then used in estimations of H_2 production per year-g rock by using a dosage rate ~$3.0 × 10^{-1}$ Gy/(yr-g rock) as calculated for 100 μg/g U and ~$2.0 × 10^{-2}$ Gy/(yr-g rock) for 1 μg/g U. The silicate mineral stopping powers of 1.5 MeV/(g-cm^{-2}), 1.25 MeV/(g-cm^{-2}), 1.14 MeV/(g-cm^{-2}) were used for alpha, beta, and gamma particles, respectively (Hofmann, 1992; Lin et al., 2005b). Simulations also included a value for low host rock porosity (0.7 %) and an average rock density of 2.73 (g/cm^{-3}) for the 95 level cores reported in

Table 1
Groundwater geochemistry and cell counts from 95 level, 101 level, 1200 level and service water fluids.

	95 Level	101 Level	1200 Level	Service Water
Depth (mbls)	3,182	3,043	1,200	2,900
T (°C)	55	45	26	22
pH	5.6	6.0	8.5	6.8
Eh (mV) SHE	161	135	174	90.0
TDS (g/L)	215	246	0.712	1.44
Water Activity	0.839	0.873	0.999	0.999
$\delta^{18}O$ (‰-VSMOW)	−11.7	−12.3	−4.0	1.1
δ^2H (‰-VSMOW)	−26.4	−22.8	−24.1	12.4
DOC (mmol/L)	8.49	23.6	0.28	0.45
$\delta^{13}C$ (‰-VPDB) DOC	−38.3	−15.7	−30.1	−55.0
DIC (mmol/L)	0.266	1.07	6.97	1.47
$\delta^{13}C$ (‰-VPDB) DIC	−13.5	−30.2	−11.6	−32.8
$^{87}Sr/^{86}Sr$	0.73349	0.73302	0.73975	n.d.
Cell Counts (cells/mL)	10^2	10^3	10^6	10^5

n.d. = no data.

Table 2
Gas compositions in % v/v for 95, 101, and 1200 level fluids.

Species	95 Level	101 level	1200 level
CH_4	45	26	26
C_2H_6	5	<1	b.d.
C_3H_8	<1	<1	<1
H_2	8	46	<1
He	22	23	14
N_2	19*	3*	47
O_2	0*	0*	2
Ar	<1*	<1*	b.d.

*values corrected for assuming modern air O_2-N_2-Ar ratios and all O_2 is from air.
b.d. = below detection.

Nkosi et al. (2022). Annual production rates for H_2, O_2, H_2O_2, and H_2O were used in Geochemist's Workbench V14 (Bethke et al., 2020) reaction with starting precursor geochemistry (Tables 1–3) and run over a period of 3.00 Ga based on high (26 % by volume) CH_4 present alongside 46 % H_2 in the 101 level gas composition (highest % by volume H_2 composition in this study). ∼70 % of produced H_2 was assumed to go into the Sabatier reaction ($4H_2 + CO_2 \rightarrow 2H_2O + CH_4$) according to reaction stoichiometry of 4:1 H_2:CH_4 (35 % going into CH_4 production and 35 % going towards the regeneration of water). Chlorinity at each time step given in mol/kg was converted to concentration in mol/L using the corresponding solvent mass at each time step (10 years), and a solution density of

1.09 g/cm³. Altering the time step to courser/finer values did not affect overall chlorinity evolution of the system.

In addition to radiolysis, the process of silicate hydration to form clays was considered for its role in salinity concentration. Here we apply a range of 3–17 % chlorite derived from the 95 level core samples (Table S3), although 1 of the 8 cores in the 101 level system did reveal a greater proportion of chlorite (80 %). The 3–17 % range was selected as it both represents the chlorite content in the lithologies most proximal to the fracture fluids, and it provides a conservative estimate of the effects of hydration reactions on the water geochemistry. The amount of H_2O sequestered annually by the hydration of mafics/ultramafics in the fracture system (necessary to produce said clay content) was estimated via the following equation:

$$H_2O\left(mol \times yr^{-1} \times L^{-1}\right) = \frac{\left(\frac{\rho_{rock} \times \%ch}{2 \times 278(g-mol^{-1})} \times 0.001\right)}{0.007 \times (2.97 \times 10^9 yr)} \quad (1)$$

Here, ρ_{rock} is the density of the rock matrix at 2.73×10^6 g-m⁻³ of rock, $\%ch$ is the fraction of chlorite based on clay estimates from LOI values according to Eq. (4) (estimated 0.03 based on 3 % minimum to 0.17 based on 17 % maximum from 95 level). In this case all clay was assumed to be chlorite. The denominator of the top fraction was obtained from Table 3 of Worden et al. (2020) and is the product of K-feldspar to H_2O stoichiometry (∼2 K-feldspar:

Table 3
Millimolar (mmol/L) concentrations for cation and anions in fracture waters and service water.

Species (mmol/L)	95 Level	101 Level	1200 Level	Service Water
Na^+	1.15×10^3	1.52×10^3	1.12×10^1	2.57×10^1
K^+	1.40×10^1	6.65	9.05×10^{-2}	5.13×10^{-1}
Mg^{2+}	3.26	2.73	3.12×10^{-1}	1.16
Ca^{2+}	1.20×10^3	1.06×10^3	6.88×10^{-1}	5.61
Si^{4+}	<1.43	<1.43	2.68×10^{-1}	2.25×10^{-1}
Mn^{2+}	1.01×10^{-1}	5.58×10^{-2}	7.38×10^{-4}	2.73×10^{-5}
Sr^{2+}	7.25	7.28	7.39×10^{-3}	2.64×10^{-2}
Total Fe	1.61×10^{-1}	3.58×10^{-2}	3.57×10^{-3}	1.08×10^{-3}
Fe^{2+}	1.15×10^{-2}	1.61×10^{-2}	1.34×10^{-3}	5.37×10^{-4}
NO_2^-	8.69×10^{-2}	1.32×10^{-2}	2.72×10^{-4}	3.59×10^{-1}
NO_3^-	1.02×10^{-1}	1.40×10^{-2}	1.55×10^{-3}	2.25
NH_4^+	1.04×10^{-1}	3.74×10^{-1}	3.40×10^{-2}	1.00×10^{-2}
SO_4^{2-}	1.25×10^{-1}	7.69×10^{-1}	6.66×10^{-1}	8.02
PO_4^{2-}	b.d.	b.d.	8.72×10^{-4}	b.d.
O_2	b.d.	4.69×10^{-2}	1.88×10^{-2}	3.75×10^{-1}
H_2S	b.d.	2.94×10^{-3}	2.94×10^{-2}	b.d.
Br^-	8.10	1.19×10^1	6.96×10^{-3}	3.81×10^{-2}
Cl^-	4.01×10^3	4.10×10^3	1.24×10^1	2.33×10^1

b.d. = below detection.

H_2O) and K-feldspar molecular weight (278 g/mol). The value 0.001 is for the conversion from m^3 to dm^3 of rock, and 0.007 is the volume fraction of pore water to rock. A chlorite formation scenario producing H_2 was not considered in this study due to the need for these reactions to occur in an olivine rich/serpentinite rich system in natural settings (Frost et al., 2008), conditions that are not found at Moab Khotsong.

2.7. Modeling the impacts of radiolysis + clay hydration on brine isotopic formation

This study considers a model for how alpha-particle-driven radiolysis may impact δ^2H of the evolution of fracture fluids along with hydrocarbon formation and clay hydration. The change in brine δ^2H over geologic time was modeled considering H mass balance for three scenarios to distinguish contribution by various water–rock processes, including: (1) contribution of H_2 by radiolysis alone, (2) contribution including H_2 and C_{1-3} alkanes, and (3) contribution of H_2, C_{1-3} alkanes, and clay hydration reactions. Mass balance for scenario (1) was calculated with the following equation:

$$\delta^2H_{brine} = \left(\frac{1}{1+\frac{f}{1-f}}\right) \cdot \left(\frac{\delta^2H_{initial}}{1-f} - \frac{f \cdot \Delta^2H}{1-f}\right) \quad (2)$$

where δ^2H_{brine} is the $^2H/^1H$ ratio of the brine, $\delta^2H_{initial}$ is the $^2H/^1H$ ratio of the brine precursor fluid (−63 ‰-VSMOW for hydrothermal fluid (Grové and Harris, 2010)) and −20 ‰-VSMOW for Precambrian seawater (Pope et al., 2012)), f is the fractional mass of H_2 species other than the brine, and Δ^2H is the fractionation factor of δ^2H-H_2 (aq) to δ^2H_{brine} at 60 °C (Pester et al., 2018; Martineau et al., 2012). A similar approach was utilized to include n species of hydrocarbons (C_{1-3} in this case) produced over time:

$$\delta^2H_{brine} = \left(\frac{1}{1+\frac{\Sigma f_n}{1-\Sigma f_n}}\right) \times \left(\frac{\delta^2H_{initial}}{1-\Sigma f_n} - \frac{\Sigma f_n \cdot \Delta^2H_n}{1-\Sigma f_n}\right) \quad (3)$$

This study considers the role of clay hydration reactions in the δ^2H-brine evolution by including interlayer H_2O accumulation for a range of non-swelling to swelling clay types, and potential mixtures thereof, including those identified through XRD for this system and in Pienaar et al. (2015). A maximum percent clay (x_1) content of 80 % was calculated using the highest LOI (%) value (y_1) from one of the 101 level cores obtained in this study (Table S3) and the linear regression relationship obtained in Tuffour et al. (2014):

$$y_1 = 0.12x_1 + 1.86 \quad (4)$$

The initial δ^2H value for clays (chlorite, illite, and smectite) used in these simulations was −50 ‰-VSMOW, falling within the observed range of δ^2H values for Witwatersrand Supergroup clays (Zhao et al., 2006). The fractional mass of each species was derived from gas analyses, and the abundance of exchangeable H_2O determined for the rock core samples by loss on ignition analyses. The change in brine δ^2H was then modeled as a function of time and increasing salinity from (1) a Precambrian seawater (1 mol/L Cl^-) and (2) a more meteoric precursor (0.5 mol/L Cl^-), to hypersaline brine (4 mol/L Cl^-). The salinity evolution over time was estimated by starting with chlorinity of the chosen precursor at time zero and subsequently dividing the salinity term by (1- f).

Alternative models were considered to see whether they could explain the observed data, including three additional scenarios: (1) a low temperature "freezing" scenario, (2) high temperature "phase separation", and (3) seawater evaporation at current brine temperature for completeness. These were determined by running evaporation paths of a modern seawater precursor to track changes in fluid Cl/Br vs Na/Br under low (0 °C), moderate (25 °C), and high

(100 °C) temperature scenarios in Geochemist's Workbench V.14 (Bethke et al., 2020). Additionally, evaporation was considered from a more saline Precambrian seawater precursor (De Ronde et al., 1997). These alternative models and discussion of their influence on the Moab Khotsong system are included in Supplementary Material (Fig. S7).

2.8. Modeling the impacts of quartz and calcite on brine isotopic formation

The influence of low temperature, low water–rock ratio equilibration on brine $\delta^{18}O$ values over geologic time was modeled by calculating the temperature-dependent isotopic fractionation $\propto_{qz-brine}(T)$ between the evolving Moab Khotsong brine and quartz, the dominant O-bearing mineral phase in Witwatersrand Supergroup quartzites, following approaches from Karolytė et al. (2017) and Warr et al. (2021) and equation (5):

$$\delta^{18}O_{H_2O=}\frac{(1000 + \delta^{18}O_{QTZ})}{\propto_{QTZ-H_2O}(T)} - 1000) \times f + \delta^{18}O_{H_2O(INIT)} \times (1-f)$$

$$(5)$$

where f is the fractional mass of brine that is in isotopic equilibrium with quartz. This calculation was repeated for calcite, another major O-bearing mineral in this system. The $\delta^{18}O$ value for quartz (10.9 ‰-VSMOW) was taken from measurements presented in Grové and Harris (2010) and Zhao et al. (2006) in addition to the highest estimated $\delta^{18}O$ value for a starting hydrothermal fluid (16.0 ‰-VSMOW) in the Witwatersrand Basin (Grové and Harris, 2010). The $\delta^{18}O$ value of the brine was taken from Warr et al. (2021). The value of calcite (10.7 ‰-VSMOW) was taken from SIMS $\delta^{18}O$ measurements from this study. Quartz and calcite equilibration was also modeled from an estimated Precambrian seawater precursor with a minimum $\delta^{18}O$ estimate of 0.8 ‰-VSMOW derived from Isua Supracrustal Belt serpentines (Pope et al., 2012). The hydrothermal maximum $\delta^{18}O$ and Precambrian seawater minimum $\delta^{18}O$ values were selected to explore mineral equilibration with brine formation from the highest and lowest possible isotopic precursor scenarios. The temperature of equilibration for brine with quartz (QTZ) and calcite (CAL) were calculated, respectively, from the following equations (O'Neil et al., 1969; Kawabe, 1978):

$$10^3\ln(\alpha_{QTZ-H_2O}) = -18.977 + 8.582(10^3/T) + 1.9189(10^3/T)^2 \quad (6)$$

$$1000\ln(\alpha_{CAL-H_2O}) = 2.78(10^6/T) - 3.39 \quad (7)$$

Progressive equilibration (0–100 % equilibrium) was modeled under a hypothetical scenario wherein mineral – water $\delta^{18}O$ exchange began at the peak greenschist facies conditions (350 °C) and progressively cooled to the current temperature of the brine system (55 °C).

Equilibrium between the brine and calcite was also modeled by calculating the fractionation factor between $\delta^{18}O$ of the brines and from calcite SIMS values. For all calculations involving SIMS data in this study, the isotopic value is provided relative to a Vienna Pee Dee Belemnite (VPDB) standard, as well as the corresponding value calculated relative to a Vienna Standard Mean Ocean Water (VSMOW) standard, due to the use of both mineral and fluid isotopic compositions. For fractionation between $\delta^{18}O$ of calcite represented in sealed veins (samples A49-6-3A and 101 level) and fluid, an $\delta^{18}O$ value of −27.8 ‰-VPDB; 2.3 ‰-VSMOW; was used. This value is the average of estimates for a Precambrian seawater precursor estimated from mineral measurements of West Greenland Isua Supracrustal Belt serpentines (Pope et al., 2012). We additionally consider a "mixed" precursor fluid scenario (part Precambrian seawater and part hydrothermal fluid) with a starting $\delta^{18}O$ value of −26.5 ‰-VPDB; 3.7 ‰-VSMOW.

Progressive brine equilibration with the $\delta^{13}C$ SIMS values from calcite veins in host rock was modeled by calculating the fractionation factor between fluid $\delta^{13}C_{CO2(aq)}$ and calcite $\delta^{13}C$ (Bottinga, 1968):

$$1000 \ln \left(\alpha_{calcite-H_2O} \right) = 2.4612 - \left(7.6663 \times 10^3 \left(T^{-1} \right) \right)$$
$$+ \left(2.988 \times 10^6 (T^{-2}) \right) \tag{8}$$

The $\delta^{13}C_{CO2(aq)}$ of the brine was obtained through inorganic carbon mass and isotopic balance provided from Geochemist's Workbench V.14 react run of fluid chemistry (Bethke et al., 2020).

3. Results

3.1. Geochemical and isotopic signatures of fracture waters

The 95 and 101 level fluids displayed high TDS (Table 1) in excess of the 35 g/L threshold required to be classified as hypersaline brine (Heath, 1983). The 1200 level at Moab Khotsong and service water salinities were much lower, showing TDS values consistent with freshwater (≤ 1.00 g/L) and the lower end of brackish fluid range (1.00–10.0 g/L), respectively (Heath, 1983). pH values of 5.6–6.0 for the brines were lower than those of the more basic dolomite aquifer at pH 8.5, while the pH of the service water was near neutral at 6.8. Temperature increased from 26 to 55 °C with reservoir depth, following a thermal gradient of 8–10 °C/km in this area of the Witwatersrand Basin (Omar et al., 2003). The lower temperature of service water (22 °C) reflected refrigerated cooling of this water by the mine (Vosloo, 2008). Eh values exceeded 100 mV for the 95, 101, and 1200 level fluids, with a slightly lower value (90.0 mV) for the service water; along with near millimolar concentrations of oxidized electron acceptor species (Table 3). These conditions may suggest microoxic redox conditions.

DOC values of 8.49–23.6 mmol/L were much higher for the brines compared to values of 0.28 mmol/L for the 1200 level sample, and 0.45 mmol/L for the service water. All samples displayed a negative $\delta^{13}C$ DOC signature with similar values for the 95 and 101 level brines ($-38.3 ‰_{-VPDB}$ and $-15.7 ‰_{-VPDB}$, respectively) relative to the 1200 level ($-30.1 ‰_{-VPDB}$), but a more negative signature in the service water ($-55.0 ‰_{-VPDB}$). DIC values showed the opposite, with higher DIC content for the service water and 1200 level samples from 1.47 to 6.97 mmol/L and a range of 0.266–1.07 mmol/L DIC for the brines. $\delta^{13}C$ DIC values for the 95 level brine and dolomite fluid were similar in signature ($-13.5 ‰_{-VPDB}$ and $-11.6 ‰_{-VPDB}$, respectively), compared to more negative values for both the service water and the 101 level brine (ranging between $-32.8 ‰_{-VPDB}$ and $-30.2 ‰_{-VPDB}$). Higher DIC values in the dolomite aquifer reflect dissolution of dolomites contributing to this aquifer (Onstott et al., 2006).

Gas compositional data (Table 2) for the air-corrected 95 level brine showed a clear dominance of reduced species: CH_4 (45 %), He (22 %), N_2 (19 %), H_2 (8 %), Ar (<1%) and volatile reduced organics (5 %) (all values by volume). The air-corrected 101 level sample displayed similar dominant species with a greater proportion as H_2 (46 %), CH_4 (26 %), He (23 %), N_2 (3 %), Ar (<1%), and volatile reduced organics (<2%). Reduced species also dominated the 1200 level sample with N_2 (47 %), CH_4 (26 %), He (14 %). The 1200 level additionally contained some O_2 (2 %).

The brines displayed similar aqueous geochemistry but were different from the dolomite aquifer and service water in terms of major cation and anion species (Table 3; Fig. 2). 95 and 101 level brines were primarily Ca-Na-Cl in composition with Ca^{2+} concentrations ranging from 1.06×10^3–1.20×10^3 mmol/L, Na^+ 1.15×10^3–1.52×10^3 mmol/L and Cl^- 3.64×10^3–4.07×10^3 mmol/L. The 1200 level sample was dominated by Na^+ and Cl^-

ions, but at concentrations 2 orders of magnitude lower than the brines. Br^- was the second most abundant anion in the brines ranging from 8.10 to 1.19×10^1 mmol/L, but the dolomite system displayed concentrations up to $\sim$3 orders of magnitude lower. Sulfate concentrations were similar across the three fluids ranging from 1.25×10^{-1}–7.69×10^{-1} mmol/L, while nitrite and nitrate concentrations were greater in the brines (1.32×10^{-2}–8.69×10^{-2} mmol/L (NO_2^-) and 1.40×10^{-2}–1.02×10^{-1} mmol/L (NO_3^-)) by up to two orders of magnitude compared to the 1200 level (2.72×10^{-4} mmol/L (NO_2^-) and 1.55×10^{-3} mmol/L (NO_3^-)). Sulfate (8.02 mmol/L) and nitrite/nitrate (3.59×10^{-1} mmol/L/2.25 mmol/L) were elevated in the service water, with this elevated nitrite/nitrate likely due to contributions from mine blasting (Silver et al., 2012). Both dissolved O_2 and H_2S values were undetectable or very low in all fluids. High strontium concentrations (7.30 mmol/L) were found in the brines relative to the 1200 level (7.36×10^{-3} mmol/L) and service water (2.64×10^{-2} mmol/L). A higher $^{87}Sr/^{86}Sr$ ratio of 0.73975 was observed for the 1200 level, compared to 0.73349 and 0.73302 for the 95 and 101 level brines, respectively (Table 1).

Stable isotopic composition of the brines showed non-meteoric signatures (Fig. 3), plotting up and to the left of the Global Meteoric Water Line (GMWL), with $\delta^{18}O$ values ranging from -11.7 to $-12.3 ‰_{-VSMOW}$ and δ^2H from -22.8 to $-26.4 ‰_{-VSMOW}$. At Moab Khotsong, the 1200 level $\delta^{18}O$ and δ^2H signature fell on the GMWL ($-4.0 ‰_{-VSMOW} \delta^{18}O$; $-24.1 ‰_{-VSMOW} \delta^2H$). Similarly, service water fell close to the GMWL, consistent with previously published data for the dolomitic aquifer (Onstott et al., 2006) from which it is likely sourced, along with some contribution from rainfall and neighboring mine treated waste waters (Vosloo, 2008). The service water signature was enriched in both $\delta^{18}O$ and δ^2H relative to the groundwater stemming from the dolomite aquifer, likely because the service water processing pipeline includes holding basins that could allow evaporative isotopic enrichment (Vosloo, 2008).

Total cell counts (Table 1) were very low in the brines with 10^2 cells/mL for 95 level and 10^3 cells/mL for 101 level. Biomass was higher in the less saline fluids, both the 1200-level dolomite fluid at 10^6 cells/mL and the 95 level service water (10^5 cells/mL).

3.2. Salinity evolution of the brine via radiolysis and clay hydration

The impact of water radiolysis on the evolution of the Moab Khotsong brines was inferred through production of radiolytic H_2 and oxidants, in addition to Cl^- increase of the fluid over time under different dosage and precursor scenarios. Considering dosage from 1 µg/g of U in the host rock, the annual yields for principal radiolytic products were $\sim$7 nmol/(L × yr) (H_2), $\sim$3 nmol/(L × yr) (O_2), $\sim$1 nmol/(L × yr) (H_2O_2), equivalent to a loss of $\sim$8 nmol/(L × yr) (H_2O). For the 100µ g/g ^{238}U scenario, annual yields were $\sim$25 nmol/(L × yr) (H_2), $\sim$11 nmol/(L × yr) (O_2), $\sim$4 nmol/(L × yr) (H_2O_2), equivalent to a loss of $\sim$26 nmol/(L × yr) (H_2O). These results suggest a $\sim$2x increase in H_2O loss nmol/(L × yr) for every 10 × increase in uranium (µg/g) and corresponding 10 × increase in alpha particle dosage rate. If the initial subsurface fluid represents Precambrian seawater (1 mol/L Cl^-) trapped in a closed system, then the resulting brine (4 mol/L Cl^-) forms within ≥ 0.45 Ga or ≤ 1.40 Ga under low and high dosage scenarios, respectively. If the precursor fluid is chosen as a low salinity, hydrothermal fluid (similar, but likely lower in starting salinity pre-radiolysis, to fluid inclusions found in fracture minerals of the Witwatersrand Supergroup ($\sim$0.5 mol/L Cl^-) (Drennan et al., 1999)), brine formation occurs within ≥ 0.50 Ga or ≤ 2.40 Ga under 1 µg/g and 100 µg/g U scenarios, respectively (Fig. 4). Also, since the true ^{238}U exposure is likely within this range, brine formation is likely close to the 1.20 Ga ^{40}Ar-derived noble gas residence time for this system (Warr
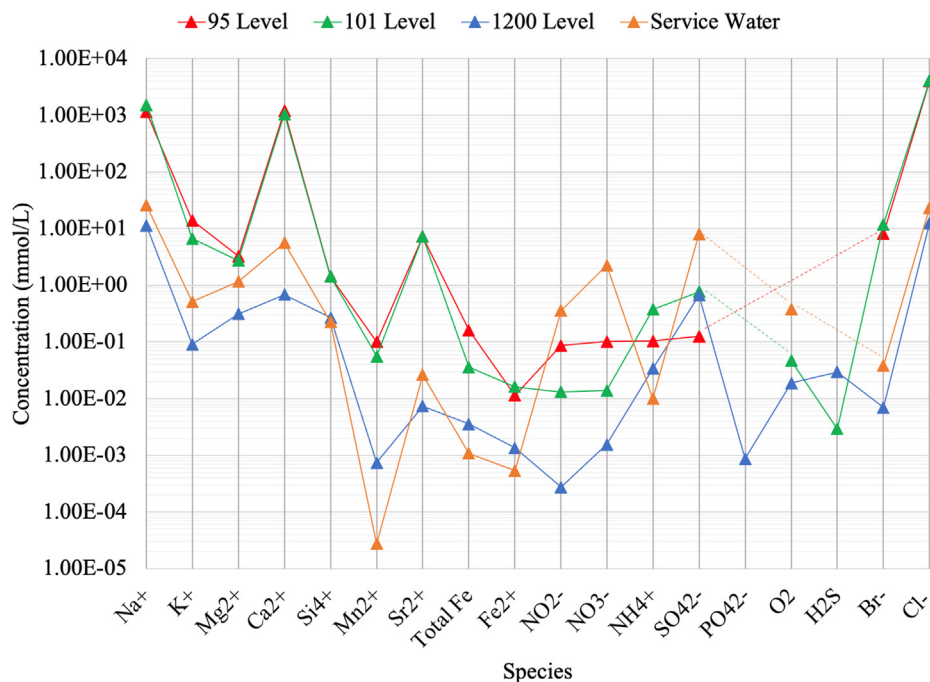
Fig. 2. Modified Schoeller diagram of major fluid species concentrations (mmol/L) presented in Table 3. Dashed lines span species whose concentration is below detection for a given fluid sample. Concentrations are taken from Table 3. Measurement uncertainties are 0.2 % (Na^+), 3 % (K^+), 20 % (Mg^{2+}), 4 % (Ca^{2+}), 15 % (Si^{4+}), 22 % (Mn^{2+}), 0.7 % (Sr^{2+}), 20 % (Fe^{2+}), 10 % (NO_2^-), 3.5 % (NO_3^-), 4 % (NH_4^+), 2 % (SO_4^{2-}), 1.7 % (PO_4^{2-}), 9 % (Br^-), 9 % (Cl^-). These are provided alongside detection limits in Table S2, and all analytical methods are described in the main text.
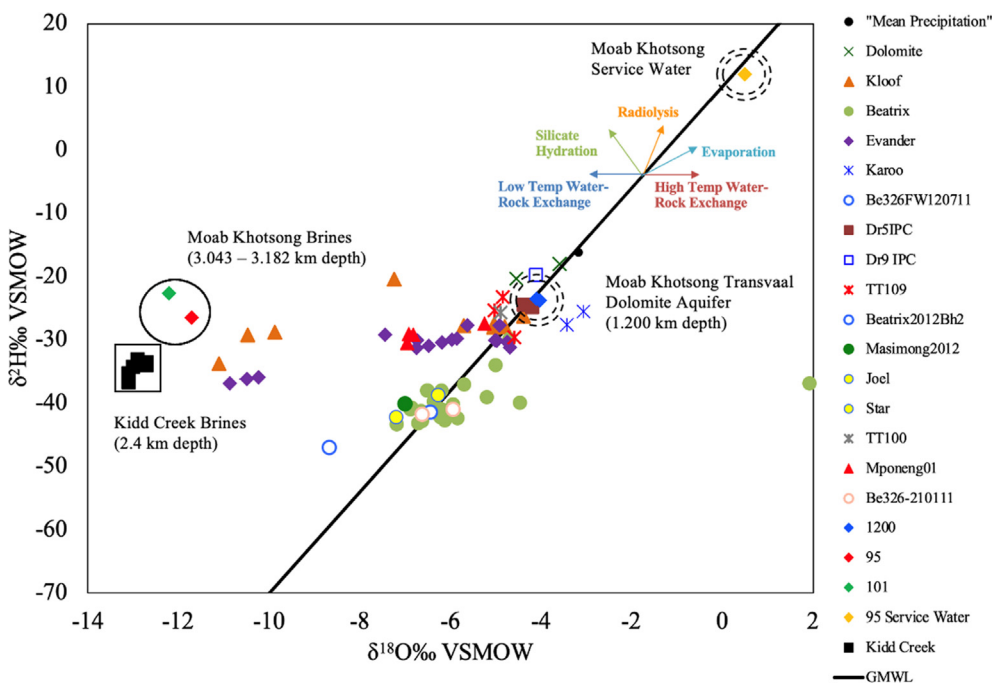
Fig. 3. Modified figure from data presented in Warr et al. (2021) of $\delta^{18}O$-H_2O and δ^2H-H_2O VSMOW signatures for Moab Khotsong brines sampled at 3.043 km depth (101 level - green diamond) and 3.182 km depth (95 level - red diamond), in addition to the dolomite aquifer from 1.200 km depth (1200 level - blue triangle) and the service water (orange diamond) (modified from Warr et al., 2021). Values from 2.4 km depth brine in Kidd Creek Mine (black squares) (Warr et al., 2018) along with other Witwatersrand Basin fracture fluids (sampled from 0.718 to 3.305 km depth) are included. Errors for δ^2H and $\delta^{18}O$ are ± 0.8 ‰ and ± 0.2 ‰, respectively, and are smaller than the symbols. (For interpretation of the references to colour in this figure legend, the reader is referred to the web version of this article.)

et al., 2022). While such hypersaline conditions can theoretically be achieved by radiolysis alone, the hydration of silicate species such as K-feldspar to form chlorite clays could contribute an additional loss of ~7 nmol/(L × yr) (3 % chlorite) to ~40 nmol/

(L × yr) (17 % chlorite) H_2O. When these two additional water loss scenarios are added to the previous radiolysis scenarios, the window over which brine formation occurs shifts only from 0.45 Ga to 2.40 Ga to 0.33 Ga–2.28 Ga.
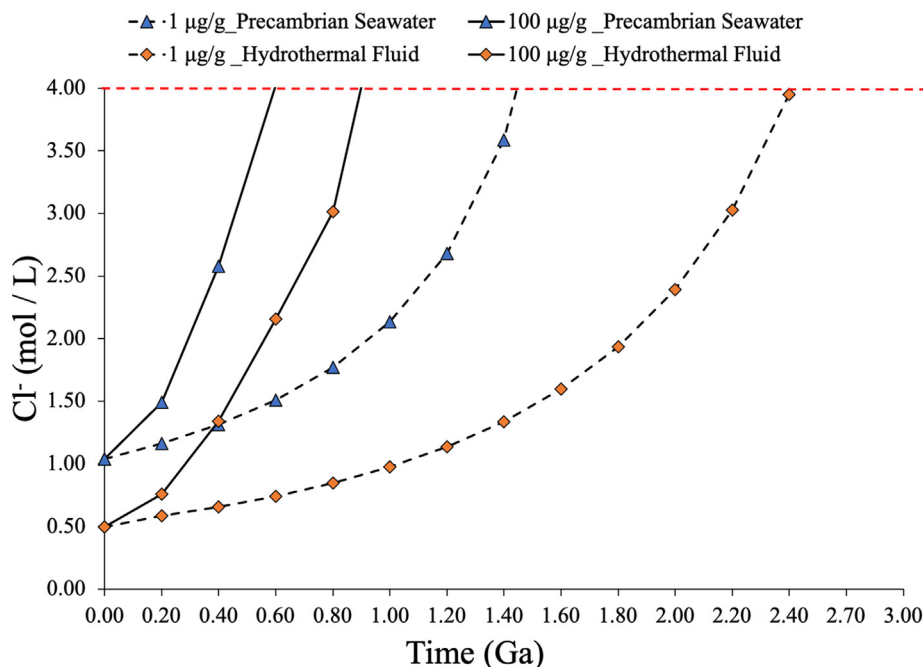
Fig. 4. Chlorinity evolution towards 4 mol/L Cl⁻ Moab Khotsong brine from low (0.5 mol/L) or high (1 mol/L) chlorinity precursors (hydrothermal fluid and Precambrian seawater respectively) under scenarios of minimum (1 µg/g ^{238}U) or maximum (100 µg/g ^{238}U) radiolytic dosage (see main text). Under all scenarios, present-day salinity levels at Moab Khotsong were generated by water–rock reaction-driven consumption of water within 0.45–2.40 Ga.

3.3. Isotopic evolution of the brine via water-rock interactions

Aside from their contribution to salinity formation over time, radiolysis and clay hydration may influence hydrogen exchange and isotopic fractionation of the fluid system over time. These two water–rock interactions (in addition to the abiotic production of C_{1-3} volatile hydrocarbon species from H_2) were considered in a mass balance between H bearing species in the system. The effect of these processes on the δ^2H_{Brine} signature was estimated over time, and it was also considered whether isotopic equilibration

with these species leads to the current day δ^2H_{Brine} signature (Fig. 5). Radiolysis acting on the system alone over evolution of the 4 mol/L Cl⁻ brine increased the fluid δ^2H signature to much heavier values ($\sim$600 ‰$_{-VSMOW}$) than the present-day brine ($\sim$−30 ‰$_{-VSMOW}$) for both fluid precursor scenarios. Such fracture fluid enrichment via radiolysis was previously suggested by a fractionation factor of α^2H_{H2O-H2} of 2.05 ± 0.07 from kinetic fractionation experiments in Lin et al., (2005b). This enriched signature was slightly diminished by the production of hydrocarbon species from the brine ($\sim$500 ‰$_{-VSMOW}$ δ^2H). The addition of clay formation in
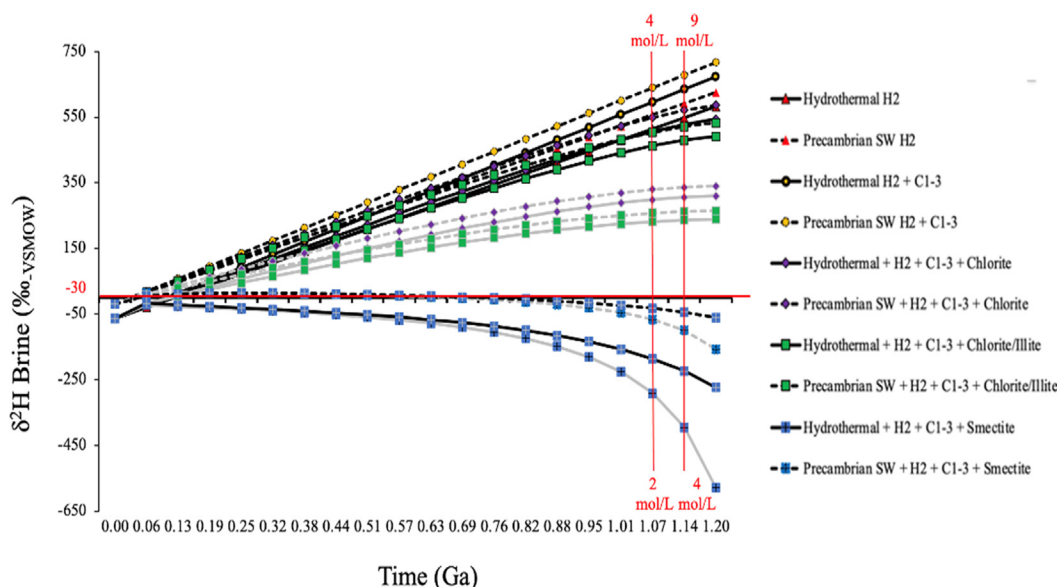
Fig. 5. Evolution of the brine δ^2H signature over time considering H mass balance scenarios with radiolytic H_2 production, volatile hydrocarbon production, and clay hydration reactions considering 3 % (black) to 17 % (grey) total clay content. Vertical red lines indicate chlorinity evolution from a Precambrian seawater precursor (top value) and from a less saline hydrothermal precursor (bottom value). Horizontal red line indicates lowest current δ^2H signature for the brines. (For interpretation of the references to colour in this figure legend, the reader is referred to the web version of this article.)

the system allowing for hydrogen exchange with interlayer and adsorbed H_2O provided an even larger diminution of the δ^2H enrichment, again due to the larger reservoir of H-bearing components considered in this mass balance scenario. This diminution effect increased for clay species capable of exchanging more H_2O, with the greatest effect provided by hydrous smectite ($\sim$−40 to −300 ‰-VSMOW δ^2H hydrothermal; $\sim$−30 to −300 ‰-VSMOW δ^2H Precambrian seawater).

XRD analysis of the 95 and 101 level cores reveal a dominance of quartz and pyrite minerals with silicates including plagioclase, actinolite, and chlorite clays (Fig. S4). The presence of quartz, calcite, pyrite, and clay minerals were confirmed with SEM/EDS analyses (Fig. S5). Four pyrite samples of 95 level borehole core displayed a $\delta^{34}S$ range of −3.90 to +4.40 ‰-VCDT (Fig. 6) but were bimodally distributed, with values falling either between −3.50 to −0.50 ‰-VCDT, or in the range of +1.80 to +4.90 ‰-VCDT. Only one core, A49-5-4.2, had all samples fall within the isotopically enriched group (+1.80 to +4.90 ‰-VCDT). The overall range for measurements of $\Delta^{33}S$ spanned −0.42 to +0.32 ‰-VCDT. SIMS microanalyses of individual crystals showed little variability in $\delta^{34}S$ and $\Delta^{33}S$ across transects (n = 4), however, each crystal displayed either exclusively positive or negative $\delta^{34}S$ values (Fig. S6).

SIMS analysis of the calcite veins and euhedral crystals in open fractures reveal a range of $\delta^{13}C$ values from −18.0 to −5.0 ‰-VPDB (12.4 to 25.8 ‰-VSMOW) and $\delta^{18}O$ values from −24.0 to −17.5 ‰-VPDB (6.2–12.9 ‰-VSMOW) (Fig. 7a and b). Within the 95 level samples, most sub-samples from each of the four cores group together with similar $\delta^{13}C$ ($\sim$−8.0 ‰-VPDB; 22.7 ‰-VSMOW) and $\delta^{18}O$ ($\sim$−19.5 ‰-VPDB; $\sim$10.8 ‰-VSMOW) signatures, with sample A49-6-3A representing a sealed vein and a more depleted signature for these two isotopes ($\sim$−18.0 ‰-VPDB; $\sim$12.4 ‰-VSMOW $\delta^{13}C$ and $\sim$−23.0 ‰-VPDB; $\sim$7.2 ‰-VSMOW $\delta^{18}O$). Samples for the combined signature for the 101 level cores ranged from −16.0 to −13.0 ‰-VPDB (14.4 to 17.5 ‰-VSMOW) for $\delta^{13}C$ and −24.0 to −22.0 ‰-VPDB (6.20–8.20 ‰-VSMOW) for $\delta^{18}O$, also representing a sealed vein. All points within a particular sample spanned a relatively narrow range of $\delta^{13}C$ and $\delta^{18}O$ signatures, with the exception of A49-6-1, which spanned a wider range of $\delta^{13}C$. Calcite $^{87}Sr/^{86}Sr$ values ranged from 0.70220 to 0.73 570.Current brine $^{87}Sr/^{86}Sr$ values (0.73302–0.73349) were more similar to the highest $^{87}Sr/^{86}Sr$ calcite signatures (Fig. 8).

Calculations of temperature-dependent $\delta^{13}C$ equilibria (Fig. 5a) between the 95 level $\delta^{13}C_{CO2(aq)}$ (−14.5 ‰-VPDB; 16.0 ‰-VSMOW) and

calcites suggested higher temperatures of equilibrium with more depleted calcites (−16.6 ‰-VPDB; 13.8 ‰-VSMOW), with progressive cooling to an equilibrium temperature consistent with the current system (55 °C) at more enriched calcite values (−7.7 ‰-VPDB; 22.9 ‰-VSMOW). The $\delta^{13}C_{CO2(aq)}$ (−99.2 ‰-VPDB; −71.4‰-VSMOW) was far too depleted for the 101 level brine to be in equilibrium with any of the measured calcites at a reasonable temperature. $\delta^{18}O$ values for the 95 level brine (−41.4 ‰-VPDB; −11.7 ‰-VSMOW) suggested similar trends, with oxygen isotopic equilibrium achieved with −19.5 ‰-VPDB; 10.8 ‰-VSMOW calcite at the current temperature of the system (Fig. 7b). In contrast, the more depleted $\delta^{18}O$ calcite values (−24.1 ‰-VPDB; 6.1 ‰-VSMOW) were consistent with equilibrium between calcite and brine at a temperature of 350 °C between sealed vein calcites and the −27.8 ‰-VPDB; 2.3 ‰-VSMOW average $\delta^{18}O$ estimate for Precambrian seawater (Pope et al., 2012). Equilibrium between the 101 level brine $\delta^{18}O$ (−41.8 ‰-VPDB; −12.2‰-VSMOW) at the current temperature of the system (45 °C) would require heavier calcite values than detected.

Fig. 9 shows a model whereby fluid-mineral interaction and related isotopic equilibration consider evolution of a single fluid body (rather than discrete fluids as in Fig. 7). When starting from a hydrothermal or Precambrian seawater precursor at 350°C, the Moab Brines reached equilibrium with quartz as well as calcite as the system cools over time (Fig. 9). This progressive equilibration resulted in $\delta^{18}O$ depletion for the brines regardless of the composition of the initial precursor. The calculated temperature of equilibration between the current brine $\delta^{18}O$ (average value of −12.0 ‰-VSMOW) with quartz was 40°C, while that for equilibrium with calcite was 52°C (Fig. 9).

4. Discussion

4.1. Geochemical and isotopic evolution of the Moab Khotsong Brine

4.1.1. Geochemical comparison to basin and global fracture fluid systems

The physiochemical and geochemical characteristics of the 95 and 101 level brines are largely distinct from the 1200 level, service water, and fracture fluid systems previously sampled in the Witwatersrand Basin. For example, pH values of 5.6–6.0 for the brines (Table 1) were lower than those of the more basic service water and dolomite aquifer (pH 6.8–8.5) as well as most other basin fluids which have neutral to alkaline values (Onstott et al., 2006);
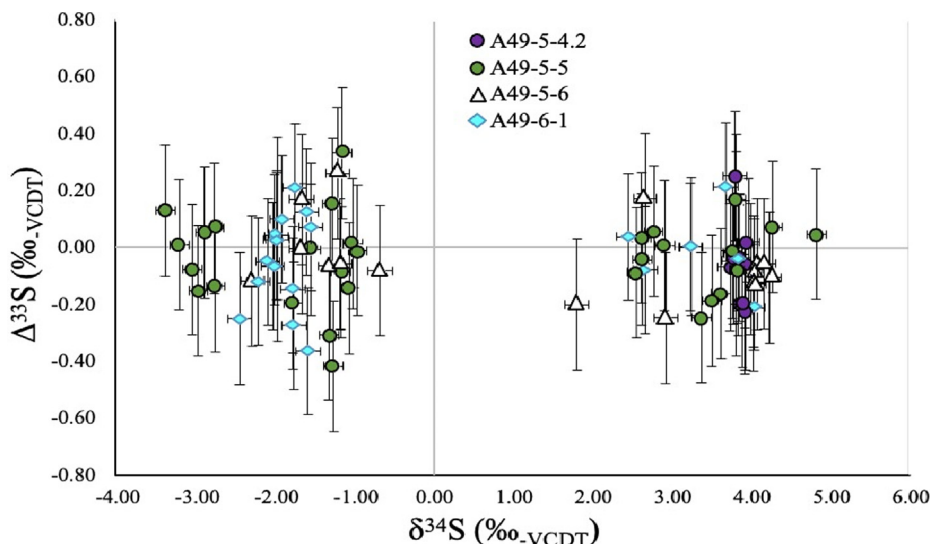

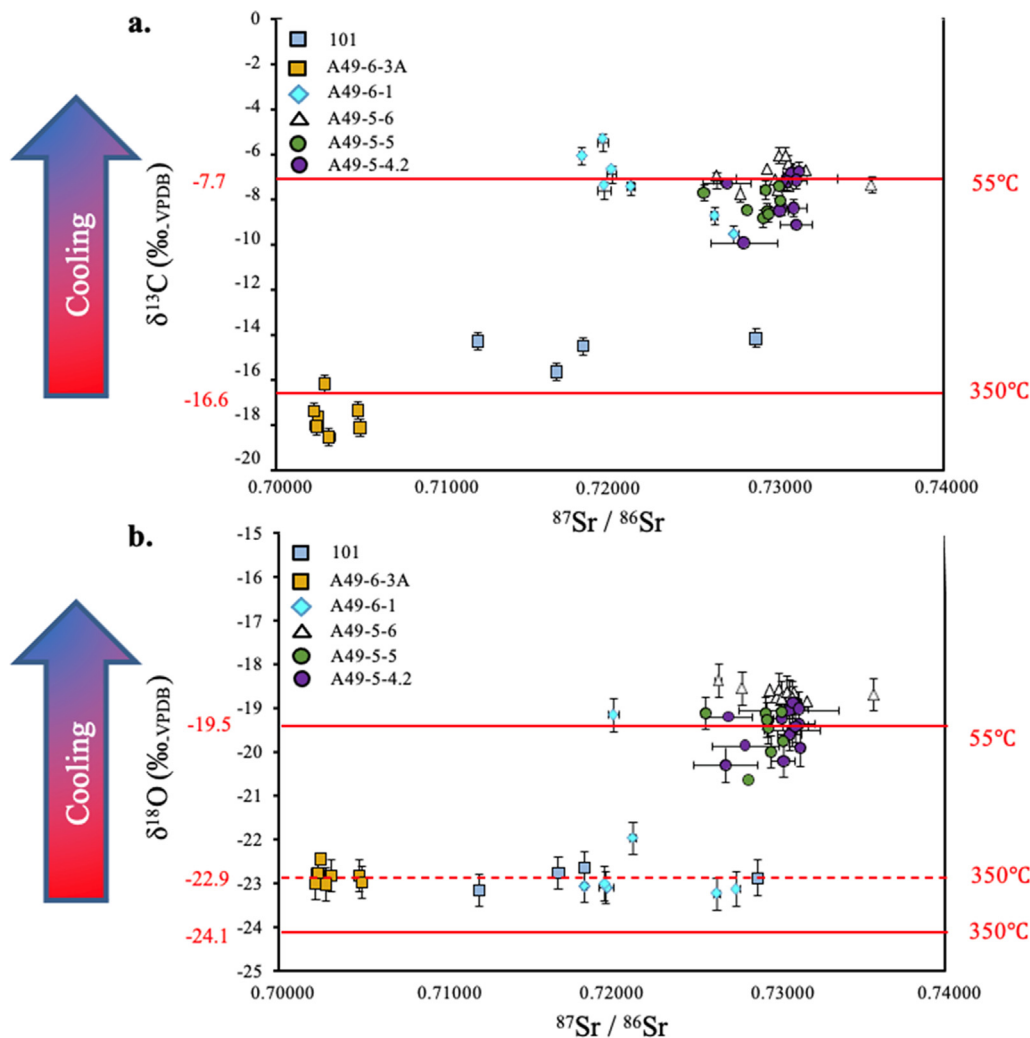**Fig. 6.** $\delta^{34}S$ vs $\Delta^{33}S$ of fracture-coating pyrite minerals for 95 level cores. Error bars represent ±1σ.

Fig. 7. (a) $^{87}Sr/^{86}Sr$ vs $\delta^{13}C$ of calcites from 95 and 101 level cores. Red lines denote values at which $\delta^{13}C_{Calcite}$ is in isotopic equilibrium with $\delta^{13}C_{CO2(aq)}$ (-14.5 ‰$_{-VPDB}$; 16.0 ‰$_{-VSMOW}$) for the peak temperature in the Witwatersrand Basin's history (350 °C) or the current temperature of the Moab Khotsong brine system (55 °C). (b) $^{87}Sr/^{86}Sr$ vs $\delta^{18}O$ measured in rock core samples. Red lines denote at which values $\delta^{18}O_{Calcite}$ is in isotopic equilibrium with $\delta^{18}O_{Precambrian\ Seawater}$ (-27.8 ‰$_{-VPDB}$; 2.3 ‰$_{-VSMOW}$) (Pope et al., 2012) for the peak temperature in the Witwatersrand Basin's history (350 °C) or with $\delta^{18}O_{Brine}$ (-41.4 ‰$_{-VPDB}$; -11.7 ‰$_{-VSMOW}$) at the current temperature of the Moab Khotsong brine system (55 °C). The dashed red line indicates equilibrium between $\delta^{18}O_{Calcite}$ and a $\delta^{18}O_{mix}$ (-26.5 ‰$_{-VPDB}$; 3.7 ‰$_{-VSMOW}$) at 350 °C. Error bars represent $\pm 1\sigma$. (For interpretation of the references to colour in this figure legend, the reader is referred to the web version of this article.)

these lower pH values appear more similar to those of 2.00–2.30 Ga hydrothermal fluid determined from fluid inclusion analyses in the basin (Drennan et al., 1999). The Eh values for the brine are more similar to shallower fracture fluid systems previously characterized in the basin (~100 mV) (Onstott et al., 2006), but there is no isotopic or geochemical evidence to suggest this is the result of fluid interaction between the brines and the 1200 level or service water (Tables 1–3; Figs. 2–3), and may reflect some *in situ* contribution of radiolytic oxidants to the brine, despite principally reducing species (Table 2). The brines additionally contained much larger organic carbon values (Table 1), exceeding the highest previously identified concentration in the Witwatersrand Basin by ~40X (Kloof Gold mine 0.410 mmol/L; Kieft et al., 2018), but were similar in $\delta^{13}C$ of DOC/DIC to the microbially dominated Kloof mine fluids (-27.5 ‰ $\delta^{13}C$ DOC/-31.5 ‰ $\delta^{13}C$ DIC, Kieft et al., 2018). The low cell counts for the brines (10^2–10^3) slightly exceeded those of Kloof mine, which maintains the lowest cell counts in the basin (~10–10^2 cells/mL) (Simkus et al., 2016) (Table 1). Dolomite estimates ~10^6 are closer to higher biomass cell counts taken from other paleometeoric fluids around the Witwatersrand Basin (Onstott et al., 2006; Pfiffner et al., 2006;

Simkus et al, 2016) and service water estimates resemble those of previous service water cell counts from mines in the Witswatersrand Basin (~10^5–10^6 cells/mL, Pfiffner et al., 2006).

High TDS (>200 g/L) values (Table 1) for the brines exceeded any previously reported salinities for fracture fluids found in the Witwatersrand Basin, the previous high being a 16 g/L fracture fluid in Kloof Mine (Onstott et al., 2006; Simkus et al., 2016; Kieft et al., 2018). Conservative anions Br^- and Cl^- for the Moab Khotsong brines demonstrates they are the most hypersaline endmembers ever sampled from the Witwatersrand Basin (Table 3; Fig. 10). Fracture and pore waters from other regions in the Witwatersrand Basin depict a strong correlation ($p = 9.19 \times 10^{-10}$) between increasing chlorinity and older age, suggesting there to be a continuum of fluids becoming more saline with residence time/hydrogeochemical isolation in the subsurface consistent with patterns found in previous studies (Lippmann-Pipke et al., 2003; Ward et al., 2004). The ancient brine end member may represent the most geochemically evolved fluid, followed by paleo-meteoric brackish intermediates, such as in the 1200 level dolomite aquifer, and finally less saline, younger meteoric fluids.
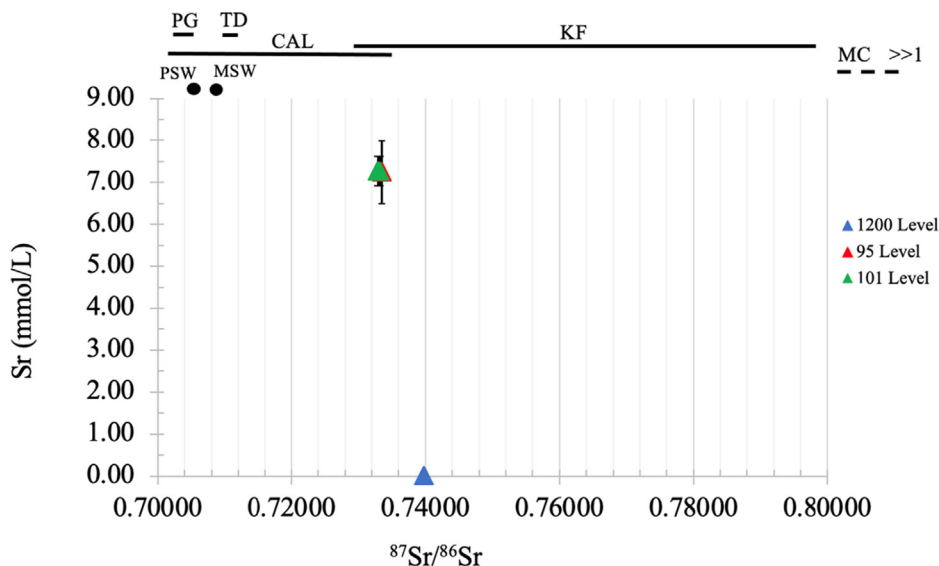
Fig. 8. $^{87}Sr/^{86}Sr$ vs Sr concentration for 95 and 101 level brines (red and green triangles, respectively) and 1200 level fracture fluid (blue triangle). Also shown are present-day $^{87}Sr/^{86}Sr$ ranges for various mineral species within the Witwatersrand Basin and Canadian Shield, for calcites presented in this study, and for Precambrian and modern seawaters. CAL = Calcites (this study), KF = K-Feldspar ([2.70 Ga] McNutt et al., 1990), PG = Ca-Plagioclase ([2.05 Ga] Wilson et al., 2017), MC = Micas ([2.70 Ga] McNutt et al., 1990; Duane et al., 1997), MSW = Modern Seawater (Peucker-Ehrenbrink and Fiske, 2019), PSW = Precambrian Seawater ([1.90 Ga] Veizer and Compston, 1976; Veizer, 1989), TD = Transvaal Dolomite ([2.19–2.64 Ga] Powell, 1962). Error bars represent ± 1. (For interpretation of the references to colour in this figure legend, the reader is referred to the web version of this article.)σ.
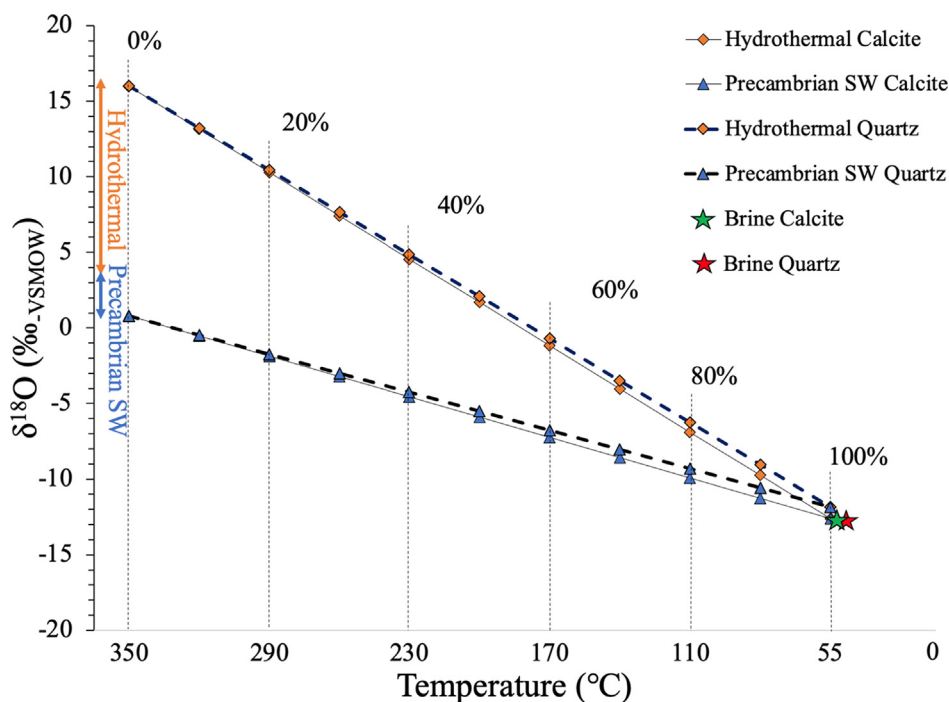
Fig. 9. Evolution of the brine $\delta^{18}O$ signature towards modern-day values with progressive cooling of the fracture system over time. Modern-day brine $\delta^{18}O$ signature at equilibrium with calcite (52 °C) and quartz (40 °C) are represented as green and red stars, respectively. Orange double-ended arrow represents the $\delta^{18}O$ range for a hydrothermal fluid precursor in the Witwatersrand Basin (Grové and Harris, 2010) while the blue double-ended arrow represents the $\delta^{18}O$ range for a Precambrian seawater precursor (Pope et al., 2012). Numerical values above the dashed lines indicate percentage of equilibration between mineral and fracture fluid at the given temperature. (For interpretation of the references to colour in this figure legend, the reader is referred to the web version of this article.)

While the brines displayed geochemical differences from fracture fluids of the Witwatersrand Basin, their geochemistry is more similar to global subsurface brines that have experienced extended hydrogeologic isolation. Such high TDS of the Moab brines were similar to values ~200 g/L from mines that include Boulby in the UK (Bottrell et al., 1996; Payler et al., 2019) and Kidd Creek on

the Canadian Shield (Lollar et al., 2019). The Ca-Na-Cl composition of the brines is consistent with Ca-Na-Cl dominance observed for other global deep subsurface fracture fluids in crystalline shields (Edmunds et al., 1987; Pearson, 1987; Blomqvist, 1999; Barth, 2000; Frape et al., 1984, 2014; Onstott et al., 2006; Stotler et al., 2009, 2010; Lollar et al., 2019; Kalwasińska et al., 2020). High
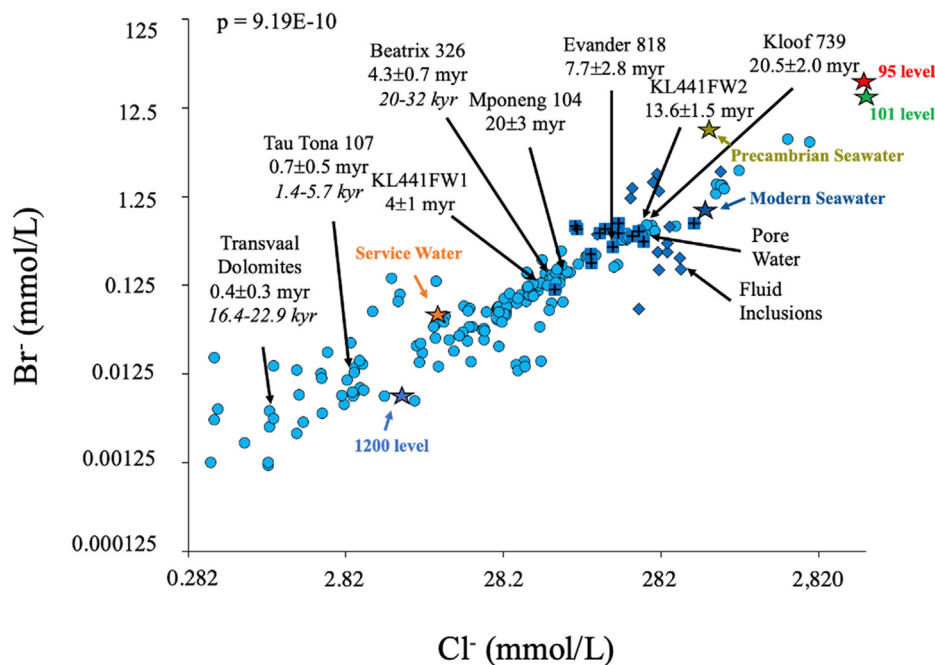
Fig. 10. Br^- vs Cl^- for Witwatersrand Basin fluid inclusions (blue diamond), pore water (blue square with black cross), Moab Khotsong Brines (red star – 95 level and green star – 101 level), and the Moab Khotsong dolomite aquifer (dark blue star – 1200 level). Witwatersrand Basin fluid subsurface residence times labeled in plain black text were determined by noble gas isotopic dating (Lippmann-Pipke et al., 2003, 2011; Heard et al., 2018) and labeled in italics were determined by $\delta^{14}C$ of DIC (Simkus et al. 2016, Borgonie et al., 2011). (For interpretation of the references to colour in this figure legend, the reader is referred to the web version of this article.)

DOC values (Table 1) are not unusual among deep subsurface brines, with many previously identified deep mine brine systems showing DOC concentrations > 2 mmol/L (Payler et al., 2019; Kalwasińska et al., 2020) and some even as high as 2.4–5 mmol/L at Kidd Creek (Sherwood Lollar et al., 2021), but the Moab brines were much more depleted in $\delta^{13}C$ DOC/DIC signatures relative to Kidd Creek (−5.1 to −8.9 ‰ $\delta^{13}C$ DOC/−0.5 to −8.8 ‰ $\delta^{13}C$ DIC, Sherwood Lollar et al., 2021). The low brine cell counts (Table 1) are close to estimates for other deep brines of the continental subsurface, including the Szczecin Trough brine in Poland ($\sim 10^4$ cells/mL, Kalwasińska et al., 2020), the Outokumpu deep drill hole ($\sim 10^3$ cells/mL, Purkamo et al., 2016; Nuppunen-Puputti et al., 2018), the lower end of Kidd Creek brine estimates ($\sim 10^3$–$\sim 10^5$ cells/mL, Lollar et al., 2019). Additionally, the dominance of reduced species in the brines (Table 2), particularly CH_4 and H_2, is consistent with deep subsurface brine systems in Precambrian cratons globally (Sherwood Lollar et al., 2002, 2006; Ward et al., 2004; Onstott et al., 2006; Kietäväinen et al., 2014; Lollar et al., 2019).

4.1.2. Salinity evolution of the Moab Brines

To form a hypersaline brine, H_2O must have been removed from the system over time contributing to increase in salinity. Here we propose that a salinity concentration mechanism in systems with low water/rock ratios may be heavily influenced by radiolysis in regions where the host minerology is rich in radiogenic species, including ^{238}U (Lin et al., 2005a; Purtschert et al., 2021). Given the potential for fluid circulation throughout the basin earlier in its thermal history, it is likely the Au-U rich Vaal reef (309–2847 µg/g U) contributed to the radiolytic evolution of the brine, which in combination with lower U values from current host rock measurements (Table S3), constrain the highest and lowest scenarios of radiogenic contribution to radiolysis-driven salinity increases, respectively (Pienaar et al., 2015). From Fig. 4, 100 µg/g of U is far higher than required to explain brine formation over the 1.20 Ga lifetime of the brine. Estimates from a 1µ g/g U contribution result in a longer time of 2.40 Ga required for brine formation

(Fig. 4), and this range suggests that radiolysis by U decay alone could account for the salinity of the hypersaline Moab Khotsong brines. This does not rule out additional contributions to water loss over time, however, such as silicate hydration considering 3–17 % clay content in the surrounding lithology, but suggests hydration reactions may play a secondary role. Even with considerations of clay hydration altering brine formation times, the true U contribution to the system likely lies within the 1 to 100 µg/g range as suggested by < 11µ g/g $^{36}Cl/Cl \times 10^{-15}$ and 20 µg/g ^{40}Ar and ^{136}Xe noble gas estimates (Warr et al., 2022) for the Moab Khotsong system, meaning there must be some contribution from a U-enriched region (such as the Vaal reef) in addition to local contribution. A similar case can be made for low and high salinity scenarios for the fluid precursor, in which a complete seawater precursor composition is not necessary for 4 mol/L Cl^- brine formation within 1.20 Ga with intermediate U values (Fig. 4).

It may be more likely that the precursor was a mixture of marine and more freshwater or hydrothermal sources, with a starting salinity of 0.5–1 mol/L Cl^-. Deposition of the West Rand Group quartzites (~ 2.97 Ga) occurred in a shallow marine environment, suggesting there could have been initial entrapment of an ancient (Precambrian) seawater precursor (Frimmel, 2019). The brine precursor may not have been simply Precambrian seawater, however, as $\delta^{13}C$ and $\delta^{18}O$ signatures for calcite veins reported in Jaguin et al. (2010) constrain a period of basin-wide fluid circulation from 2.64 Ga to 2.43 Ga, flowing from above the Chuniespoort Group to further down in the stratigraphy, potentially reaching the West Rand Group along regions of high permeability. In this case, Jaguin et al. (2010) suggests the permeating fluid may not have been exclusively marine in origin. A less saline hydrothermal fluid could have mixed with entrapped Precambrian seawater in the West Rand, if present, forming a partial marine precursor that (with subsequent meteoric contribution up to ~ 2.00 Ga due to a thermal spike caused by the Vredefort meteorite impact) would evolve *in situ* to result in the hypersaline Moab brine per the model proposed here. Given that the 1.20 Ga residence time for this system

is a conservative estimate, the precursor may have exceeded this age.

4.1.3. Isotopic evolution through equilibration

The effect of extended water–rock interaction on this system can also be seen in the evolution of brine isotopic signatures over time. For salinity and isotopic signatures of the brine to evolve over Ga timescales through water–rock interaction, the brine must have been hydrogeologically isolated over an appropriately long time period in a fracture system of low porosity and permeability. Both the matrix porosity (0.38–0.91 %) (Table S3) and permeability values (fracture: 1.11×10^{-15}–9.31×10^{-16} m^2; bulk: 5.82×10^{-19}–1.27×10^{-18} m^2) (Table S7) for ~3.0 km depth in the West Rand Supergroup agree with low bulk porosity measurements from other studies of crystalline rocks and with permeability estimates at similar depths previously modeled for the Canadian and Fennoscandian Shields (0.1 to 2 %; Farvolden et al., 1988; Nordstrom et al., 1989; Stober and Bucher, 2007; Sherwood Lollar et al., 2014 and references therein). The presence of high-density sills on either side of the brine contact zone (Fig. S1b) present regions of particularly low permeability and relative stability, likely contributing to the lasting rigidity of the borehole over long time scales, including that post drilling (Nkosi et al., 2022). Additional support for the relative hydrogeologic isolation of the brine can be seen in pressure fluctuations over time for the 95 level borehole (Fig. S8) which are typical of rigid, hard rock groundwaters at depth subjected to Earth tidal oscillations (Maréchal et al., 2002). Pumping, blasting, and evapo-transpiration induced fluctuations can be negated in Fig. S8 based on the location, depth, and accessibility of the mine site (Fig. S1a). Higher permeability dykes can be found in Moab Khotsong extending from 2.6 to 3.2 km (Fig. S1a), but it is still unclear whether these may intersect the brines at some point. Any fluid circulation/mixing that could occur if the brine bearing formation was intersected would be confined within these depths, preventing the potential for mixing of the brine with shallower paleometeoric sources such as the 1200 level at 1.2 km.

With this knowledge of a low porosity/permeability system at Moab, one isotopic indicator that can be used to evaluate the effect of water–rock interaction on a long-isolated system is δ^2H evolution of the brine (Fig. 5). While the formation of hydrous clays allowing H$_2$O exchange contributes to the expected change in δ^2H for this brine, this is very dependent on clay type and clay content of the host rock. Even if clay content was extended to a maximum estimate of 80 % (a high percentage found in one section of the 101 level core), the final δ^2H would be too enriched if only considering chlorite clays identified in this study, and a large contribution of smectite would be required to buffer the brine down to -30 ‰$_{\text{-VSMOW}}$ within 1.20 Ga. Additionally, such a high clay content does not agree with low porosity and permeability estimates for this system (Table S3; Table S7). Although the addition of clay minerals observed in core lithology from this study do not dampen the increasing δ^2H$_{\text{brine}}$ enrichment enough to be comparable with that observed in the present-day, the appearance of hydrated clays, including muscovite, commonly occur with chlorite/illite transitions, with illite and muscovite previously reported in Moab Khotsong rock analysis (Pienaar et al., 2015).

In such a low porosity/permeability system such as occurs in the West Rand of Moab Khotsong, the potential for recent or current fluid recharge is small. A closer look at mineral grains such as pyrite, however, may help constrain the relative timing of fluid flow events. δ^{34}S values span a range of ~± 5 ‰$_{\text{-VCDT}}$ which has been associated with pyrite grains in fluvial plain deposits of the West Rand group, displaying a mass dependent fractionation (MDF) crustal signature (Guy 2012a; Guy et al., 2012b; Guy et al., 2014). Mixing between an atmospheric S reservoir of mass independent fractionation (MIF) signature, with a MDF crustal S

reservoir, could account for both Δ^{33}S and δ^{34}S variations for the Moab Khotsong pyrites (Guy 2012a; Guy et al., 2012b; Guy et al., 2014); it should be noted, however, that the error on Δ^{33}S measurements in this study do not allow for a confident determination in MIF signature (Fig. 6). The clearly bimodal distribution in pyrite δ^{34}S and lack of overlapping signatures between the two groups suggests two discrete fluid flow events. The more enriched δ^{34}S group (Fig. 6) may represent contribution from a MDF marine S reservoir, instead of a crustal reservoir (Guy 2012a; Guy et al., 2012b; Guy et al., 2014). If these two groups were indeed due to discrete fluid flow events, then the group more depleted in δ^{34}S could represent an earlier fluvial pyrite origin, followed by a second marine pyrite origin representing the more enriched δ^{34}S group (Guy 2012a; Guy et al., 2012b; Guy et al., 2014). Alternative explanations could be considered for alteration of δ^{34}S values that do not rely primarily on fluid origin, including contribution from microbial reduction of sulfate or elemental sulfur reduction. Microbial reduction could lead to depletion in δ^{34}S over time, but this trend is unlikely, given the lack of intermediate δ^{34}S values between the two groups and a slightly narrower Δ^{33}S range than is typically associated with these processes (Philippot et al., 2007). The lack of intermediate δ^{34}S values is additionally unusual if considering thermochemical sulfate reduction, TSR, or Rayleigh distillation processes. TSR could be considered to contribute intergroup variation in δ^{34}S, but this is not consistent with the paucity of H$_2$S in the system (Table 3).

A more complete picture of the brine hydrogeologic history is revealed when considering the evolution of δ^2H and δ^{18}O of the fluid over time relative to the host rock. Analysis of authigenic quartz, calcite and muscovite isotopic signatures in the VCR by Zhao et al. (2006) and in the bulk Carbon Leader Reef (the major gold— and uranium— bearing reef in Witwatersrand Basin's Carlton mining district (Robb and Robb, 1998)) by Grové and Harris, (2010) led them to suggest the δ^2H and δ^{18}O values they observed were consistent with a 2.00–2.20 Ga hydrothermal precursor fluid in equilibrium with these minerals at 350 °C, plotting to the right of the GMWL. Subsequent processes contributing to more depleted δ^{18}O values and a shift to the left of the GMWL (Fig. 3), they suggest occurred as the stratigraphy cooled from peak greenschist facies conditions and δ^{18}O exchange between dominant O bearing minerals and the fluid continued over long timescales as similarly suggested by Kieft et al. (2005), Onstott et al. (2006), and Warr et al. (2021).

The depleted δ^{18}O values for the brines relative to meteoric fluids are much more negative than for previously reported Witwatersrand Basin fracture fluids (previous range of ~-12.0 to ~ 2.0 ‰$_{\text{VSMOW}}$) (Fig. 3) (Warr et al., 2021). The Moab Khotsong brines additionally showed a δ^2H enrichment up to +4 ‰ relative to Kloof Mine fluids, which displayed the most positive δ^2H signature among Witwatersrand Basin values reported in Warr et al. (2021). This shift in δ^{18}O to more negative values in the brines suggests that younger Witwatersrand Basin fracture fluid systems will follow a similar trend with continued low temperature isotopic exchange with O bearing minerals; this shift can be seen in the previously oldest and most saline fluids of Kloof Mine in (Fig. 3). An increase in δ^2H would only be expected for radionuclide-rich aquifers in the basin (e.g. proximal to U-bearing gold reefs) or in clay rich zones, conditions which are particularly elevated at Moab Khotsong. Compared to global fluids, the negative δ^{18}O of the Moab brines is similar to brines at Kidd Creek on the Canadian Shield, the only other global brines to have experienced a comparable > 1.00 Ga subsurface residence time. Kidd Creek δ^2H values are not as heavy, however, but this is likely due to increased radionuclide concentrations in the Moab system.

In this study, the $\delta^{18}O$ and $\delta^{13}C$ signatures provided by SIMs analyses of calcites in the surrounding rock cores (Fig. 7) provide a closer look at equilibration as the system cooled from peak greenschist facies conditions. When considering the average $\delta^{18}O$ estimated for a Precambrian seawater precursor (-27.8 ‰-VPDB; 2.3 ‰-VSMOW), equilibrium with calcites more depleted in $\delta^{18}O$ relative to other calcites in the Moab system (-24.1 ‰-VPDB; 6.1 ‰-VSMOW) would have occurred at 350 °C (Fig. 7). There is even stronger support for a partial marine precursor considering a starting $\delta^{18}O$ fluid value of -26.5 ‰-VPDB; 3.7 ‰-VSMOW, in which the fluid would achieve equilibrium with -22.9 ‰-VPDB; 7.3 ‰-VSMOW calcites at 350 °C, providing an even better agreement with the lightest calcite signatures in this study. The lighter isotopic values for these calcite samples indicate their deposition during an earlier period of rock-water equilibration preserved as fracture minerals. This early fluid-rock interaction would precede the main brine formation, or may be a partial component of a larger fluid precursor composition that went on to participate in ^{18}O equilibration with quartz and calcite throughout the lifetime of the brine. A look at $\delta^{18}O$ from calcite veins of fluid inclusions in Orkney (Jaguin et al., 2010), with values of -22.4 to -21.0 ‰-VPDB; 7.9–9.3 ‰-VSMOW and homogenization temperatures of 130–200 °C in Orkney and Welkom, suggest these inclusion fluids may represent a slightly younger fluid than the oldest precursor for the brines (also supported by fluid inclusion position in Fig. 10), as it would need a more negative $\delta^{18}O$ to be at equilibrium with these calcites within the homogenization temperature range. Equilibrium with $\delta^{13}C$ depleted calcites (-16.6 ‰-VPDB; 13.8 ‰-VSMOW) and the current brine $\delta^{13}C$ (-14.5 ‰-VPDB; 16.0 ‰-VSMOW) additionally support equilibrium temperatures of ~350 °C. Cooling from such a high temperature to modern day values is consistent with formation temperatures for additional minerals identified in XRD analysis of the 101 level core, including actinolite (Inoue et al., 2010) and chlorite (Coombs et al., 1976). Whether or not the precursor was seawater, hydrothermal fluid, or a mixture, $\delta^{18}O$ equilibrium temperatures between the Moab Khotsong brines (-12.0 ‰-VSMOW) and quartz (10.9 ‰-VSMOW) or calcite (10.7 ‰-VSMOW) of 40 °C and 52 °C, respectively, suggest any precursor fluid was significantly altered by water–rock interaction as the system cooled (Fig. 9).

Evolution of the system is further supported by apparent shift in Sr isotopic signature of the fluid and surrounding rock. If the precursor fluid contained components of ancient seawater, it would have had a lower signature similar to $^{87}Sr/^{86}Sr = 0.7025$ for Archaean carbonates that buffered ~2.9 Ga Precambrian oceans (Fig. 8) (Veizer. And Compston, 1976; Veizer et al., 1989), and must have acquired Sr contribution from surrounding rock over time. $^{87}Sr/^{86}Sr$ isotopic values presented for calcites in this study reflect the change in Sr isotopic signature as the system cooled from 350 °C to the current temperature of 55 °C (Fig. 7), but were likely not the main contributors to the fluid signature. Other potential contributors (Fig. 8) include 2.70 Ga K-feldspars that have been identified in the Witwatersrand Basin (Pienaar et al., 2015) with current Sr isotope ratios of 0.730–0.800 (McNutt et al., 1990), as well as mica clays including chlorite species with present-day Sr isotope ratios ≫1 (McNutt et al., 1990; Duane et al., 1997). This water–mineral exchange and mineral isotopic buffering assume that the rock/water ratio in the system remained high since the time of this greenschist metamorphism (~2.00 Ga), as reported by Jaguin et al. (2010), and is consistent with the > 1.00 Ga fluid residence times calculated for this system (Warr et al., 2022). The contrasting high Sr ratio and low Sr concentration in the 1200 level fluid may reflect some contribution from dolomite (Fig. 8), whose mineral structure contains more of the parent isotope ^{87}Rb, but is likely derived from ^{87}Rb-rich chloritic micas along the flow path (Button, 1975; McNutt, 2000; Nebel et al., 2011).

4.2. Implications for past and present microbial habitability

4.2.1. Water-rock contribution to electron acceptor/donor availability

The decay of U, Th, and K is responsible, via radiolysis, for the production of electron donor H_2 and of oxidants H_2O_2 and O_2 in the Moab brines. The free oxidant concentrations are low to non-detectable in the 95 and 101 level brines, suggesting their subsequent reactivity with reduced species, or their quick utilization by inhabiting biota; this consistent production and quick utilization may be responsible for the microoxic conditions in the brine, despite low O_2 detection. Such reactions may include the production of electron acceptors ferric iron and sulfate from the oxidation of pyrite (Li et al., 2016), and nitrite/nitrate from the oxidation of ammonia/ammonium that may be released via cation exchange from host rock phyllosilicates, and simple inorganic and organic carbon molecules such as DIC and methane with the potential to form additional VOC's and VFA's (Sherwood Lollar et al., 2021) (Fig. 11). Additionally, there can be radiolytic production of N_2 via the formation of an N_2O intermediate (Karolytè et al., 2022), adding to an abiotic N cycle. The contribution of NH_3 via N_2 fixation is unresolved, however, due to the potential for various abiotic/biotic mechanisms. Finally, phosphate concentration was below detection in the brines, and its concentration likely constrained by the precipitation of hydroxyapatite (Fig. S9).

4.2.2. Initial Implications for habitability and comparison to global habitable brines

This study supports the Moab Khotsong brine as having a long history of hydrogeochemical isolation and extended influence from abiotic water–rock interaction contributing to a seemingly closed redox and nutrient landscape with an extant microbial community of very low biomass (10^2 cells/mL). These characteristics are not shared with previously explored Witwatersrand Basin fluids, whose salinities and ages have previously not been found to exceed 100,000 mg/L and 100 Ma, respectively (Lippmann-Pipke et al., 2003; Onstott et al., 2006; Lau et al., 2014; Simkus et al., 2016; Heard et al., 2018; Kieft et al., 2018). Looking at the thermal history of the basin, microbial life would not have survived prior to (or during) peak greenschist facies conditions, constraining micro-
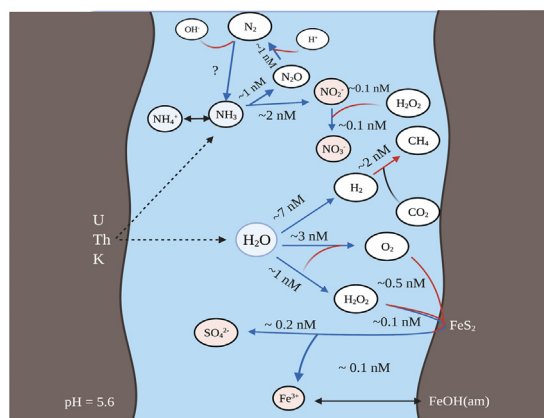

Fig. 11. Illustration of electron donor/acceptor formation rates in nM (nmol/ (L × yr)) in the 95 level brine due to water–mineral interactions including radioactive decay from the host rock (figure created with BioRender.com). This includes ~10 % of each radiolytic oxidant contributing to pyrite oxidation (Dos Santos et al., 2016), ~10 % conversion of NH_3 to NO_2^- (Silver et al., 2012), and ~4 % of NO_2^- oxidized to NO_3^- (Shin et al., 2001). Radiolytic contribution pathway of N_2 is also included (Karolyté et al., 2022). This figure considers the lowest dosage scenario (1 μg/g U). Abiotically generated electron acceptors are shown in orange circles. (For interpretation of the references to colour in this figure legend, the reader is referred to the web version of this article.)

bial infiltration to fluid mixing some time after conditions cooled below 100 °C. This is consistent with thermochronological constraints placed on habitability of near surface regions of Precambrian shield sites, including the Kaapvaal Craton in South Africa, where potential periods of habitability are constrained to windows < 100 °C and suggest multiple possible recolonization events (Drake and Reiners, 2021). One scenario is that there was mixing of a younger paleometeoric fluid with the brine system at some point during its formation history. Additionally, there could be current mixing with such a fluid (to such a minor extent it is not reflected in the brine geochemistry), which could contribute halophilic and or thermophilic members capable of sustaining populations in the extreme conditions of the brine. Such a scenario would be consistent with patterns of fluid mixing promoting habitability at other sites in the Witwatersrand Basin (Lin et al., 2006; Borgonie et al. 2019) but this study would be the first to observe this phenomenon for such hypersaline and ancient fluids.

The low biomass hypersaline Moab Khotsong brines appear more similar to the 1.70 Ga brines from Kidd Creek within the Canadian Shield, where abiotic water–rock processes dominate the fracture fluids. In the case of Kidd Creek, this includes abiotic production of H_2 from processes including radiolysis and serpentinization, and abiogenic production of hydrocarbons C_{1-4}, acetate, and formate (Sherwood Lollar et al., 2002, 2008, 2021; Young et al 2017; Warr et al., 2019). The Moab Khotsong brine has the highest concentrations of radiogenic noble gas products, including the highest excesses of $^{131-136}Xe$ and ^{86}Kr ever reported in the literature (Warr et al., 2022), This is additionally reflected in a large H_2 contribution from radiolysis (5–17 nmol/(L × yr) H_2 produced after accounting for methane production) with the potential to sustain long-term H_2 availability for chemolithotrophic microbial metabolisms. Specific estimates for steady-state aqueous H_2 have been previously associated with chemolithotrophic strategies including: microbial nitrate reduction (0.05 nmol/(L × yr)), sulfate reduction (1–1.5 nmol/(L × yr)), and methanogenesis (7–10 nmol/(L × yr)) (Lovley and Goodwin, 1988). These amounts suggest annual radiolytic production of H_2 (and oxidants) in the Moab Khotsong brines is sufficient to support H_2 utilizing chemolithotrophic life, but may support even more diverse H_2 utilizing communities under higher radiolysis scenarios than that of Fig. 4. This could additionally provide H_2 contribution to low level abiotic hydrocarbon production similar to Kidd Creek (Sherwood Lollar et al., 2002; Warr et al., 2021). With radiolytic H_2 production, electron acceptor production, and the potential abiotic production of reduced carbon species, severe phosphate limitation may remain as the primary constraint on microbial growth for this system (Fig. S9) although resolving this critical question is outside the scope of this study. Nevertheless, considering the abundance of H_2 as an electron donor, candidate metabolic strategies may involve the use of any available excess O_2, nitrite/nitrate, sulfite/-sulfate, or ferric iron as electron acceptors, which are also present at appreciable amounts in the Moab Khotsong brine system. Additionally, given the large DOC pool of the Moab Khotsong brines and potential for abiotic e- acceptor species production, chemoorganotrophy may be favored alongside or in preference to chemolithotrophic strategies and should be considered as a natural metabolic process given the system over geologic time.

5. Conclusions

The Moab Khotsong brines display geochemical and isotopic signatures that are consistent with those of global Precambrian Shield brines that have been altered significantly by water–rock interactions over geologic time, but are distinct from other fracture fluid systems previously analyzed in the Witwatersrand Basin as

well as younger dolomitic and service waters in the mine. Comparison of geochemistry including Cl^- and Br^- suggests the brines position as a hypersaline fluid of potentially ancient marine origin, identifying for the first time, an extreme end-member among a continuum of younger brackish paleo-meteoric intermediates to more meteoric fluids found throughout the Witwatersrand Basin. The high uranium concentration within Moab Khotsong and rates of radiolytic water removal over time (along with contribution from clay hydration reactions) can account for the increasing salinity of these fluids over a ~1.20 Ga period via radiolysis acting on a partial marine, hydrothermal precursor. Over time, these radiolytic reactions supplied H_2 that fueled subsequent abiotic production of reduced gases, and oxidants including O_2 and H_2O_2 that were available for potential use by microbes and to supply small quantities of alternative electron acceptors (NO_2^-, NO_3^-, SO_4^{2-}, Fe^{3+}). Concentrations of major cations and anions reflect longstanding fluid interactions with host rock species including quartz, calcite, and pyrite. Stable isotopic signatures of quartz, calcite, and pyrite, in addition to calcite $^{87}Sr/^{86}Sr$ signatures, suggest isotopic equilibrium between these minerals and the current brines have been reached over the long cooling history of the basin and control the observed isotopic signatures, to a large degree overprinting elemental signatures. Other low temperature water–rock interactions include the alteration of anhydrous silicates to clays, including chlorites, which helped buffer the δ^2H signatures of the brines as it increased under continuous radiolysis. The accumulation of potential electron donor/acceptor species over geologic time suggests the current low biomass community of the brines may involve chemoorganotrophic or chemolithotrophic strategies dependent on an abiotically dominated geochemical system. The extreme history and composition of the Moab Khotsong brine system suggest its value as an analog for microbial habitability in extraterrestrial settings. Further investigation of ancient deep brines like that of Moab Khotsong will aid in exploration for potential habitability in the subsurface of Mars (Tarnas et al., 2021) or putative ocean satellite moons, including Europa (Chyba and Phillips, 2001) and Enceladus (McKay et al., 2014), where there is initial evidence for abiotic redox and carbon environments with limited surficial input.

Appendix A. Supplementary material

Supplementary material to this article can be found online at https://doi.org/10.1016/j.gca.2022.11.015.

References

Barth, S.R., 2000. Geochemical and boron, oxygen and hydrogen isotopic constraints on the origin of salinity in groundwaters from the crystalline basement of the Alpine Foreland. Appl. Geochem. 15, 937–952.

Barton, C.D., Karathanasis, A.D., 2002. Clay minerals. In: Lal, R. (Ed.), Encyclopedia of Soil Science. 2nd ed. Marcel Dekker Inc., New York, pp. 187–192.

Bethke, C.M., Farrell, B., Sharifi, M., 2020. The Geochemist's Workbench Release 14. Gwb Essentials Guide. Aqueous Solutions LLC., Champaign, IL, USA.

Bjergbakke, E., Dragarne, Z.D., Sehested, K., Dragarne, I.G., 1989. Radiolytic products in waters. Radiochim. Acta. 48, 65–72.

Blomqvist, R., 1999. Hydrogeochemistry of deep groundwaters in the central part of the Fennoscandian Shield. In: Geological Survey of Finland, Nuclear Waste Disposal Research, Report (No. GTK-YST-101). pp. 3–37.

Blyth, A., Frape, S., Blomqvist, R., Nissinen, P., 2000. Assessing the past thermal and chemical history of fluids in crystalline rock by combining fluid inclusion and isotopic investigations of fracture calcite. Appl. Geochem. 10, 1417–1437.

Blyth, A., Frape, S., Ruskeeniemi, T., Blomqvist, R., 2004. Origins, closed system formation and preservation of calcites in glaciated crystalline bedrock: evidence from the Palmottu natural analogue site, Finland. Appl. Geochem. 5, 675–686.

Blyth, A.R., Frape, S.K., Tullborg, E.L., 2009. A review and comparison of fracture mineral investigations and their application to radioactive waste disposal. Appl. Geochem. 5, 821–835.

Borgonie, G., Magnabosco, C., García-Moyano, A., Linage-Alvarez, B., Ojo, A.O., Freese, L.B., Van Jaarsveld, C., Van Rooye, N.C., Kuloyo, O., Cason, E.D., Vermeulen, J., 2019. New ecosystems in the deep subsurface follow the flow of water driven by geological activity. Sci. Rep. 9, 1–16.

Borgonie, G., García-Moyano, A., Litthauer, D., Bert, W., Bester, A., van Heerden, E., Möller, C., Erasmus, M., Onstott, T.C., 2011. Nematoda from the terrestrial deep subsurface of South Africa. Nature 474, 79–82.

Bottinga, Y., 1968. Calculation of fractionation factors for carbon and oxygen isotopic exchange in the system calcite-carbon dioxide-water. J. Phys. Chem. 72, 800–808.

Bottomley, D.J., Gregoire, D.C., Raven, K.G., 1994. Saline ground waters and brines in the Canadian Shield: geochemical and isotopic evidence for a residual evaporite brine component. Geochim. Cosmochim. Acta 5, 1483–1498.

Bottrell, S.H., Leosson, M.A., Newton, R.J., 1996. Origin of brine inflows at Boulby potash mine, Cleveland, England. Trans. Inst. Min. Metall. B 105, 159–164.

Braun, J., Guillocheau, F., Robin, C., Baby, G., Jelsma, H., 2014. Rapid erosion of the Southern African Plateau as it climbs over a mantle superswell. J. Geophys. Res. Solid Earth 119, 6093–6112.

Buck, E.C., Wittman, R.S., Skomurski, F.N., Cantrell, K.J., McNamara, B.K., Soderquist, C.Z., 2012. Radiolysis Process Modeling Results for Scenarios, in: PNNL-21554 report FCRD-UFD-2012. pp.199.

Button, A., 1975. Geochemistry of the Malmani Dolomite of the Transvaal Supergroup in the northeastern Transvaal. Econ. Geol. Res. Unit 97, 1–21.

Cabral, R.A., Jackson, M.G., Rose-Koga, E.F., Koga, K.T., Whitehouse, M.J., Antonelli, M.A., Farquhar, J., Day, J.M.D., Hauri, E.H., 2013. Anomalous sulphur isotopes in

plume lavas reveal deep mantle storage of Archaean crust. Nature 496, 490–493.

Carpenter, A.B., 1978. Origin And Chemical Evolution Of Brines In Sedimentary Basins. Okla. Geol. Surv. Circ. 79, 60–77.

Catuneanu, O., Biddulph, M.N., 2001. Sequence stratigraphy of the Vaal Reef facies associations in the Witwatersrand foredeep, South Africa. Sediment. Geol. 141, 113–130.

Charlou, J.L., Donval, J.P., Fouquet, Y., Jean-Baptiste, P., Holm, N., 2002. Geochemistry of high H_2 and CH_4 vent fluids issuing from ultramafic rocks at the Rainbow hydrothermal field (36 14' N, MAR). Chem. Geol. 191, 345–359.

Chen, Y., Lehmann, K.K., Kessler, J., Sherwood Lollar, B., Couloume, G.L., Onstott, T.C., 2013. Measurement of the $^{13}C/^{12}C$ of atmospheric CH_4 using near-infrared (NIR) cavity ring-down spectroscopy. Anal. Chem. 85, 11250–11257.

Chyba, C.F., Phillips, C.B., 2001. Possible ecosystems and the search for life on Europa. Proc. Natl. Acad. Sci. U.S.A. 98, 801–804.

Coombs, D.S., Nakamura, Y., Vuagnat, M., 1976. Pumpellyite-actinolite facies schists of the Taveyanne Formation near Loèche, Valais, Switzerland. J. Petrol. 17, 440–471.

Crowe, D.E., Vaughan, R.G., 1966. Characterization and use of isotopically homogeneous standards for in situ laser microprobe analysis of $^{34}S/^{32}S$ ratios. Am. Mineral. 81, 187–193.

De Ronde, C.E., Channer, D.M.D., Faure, K., Bray, C.J., Spooner, E.T., 1997. Fluid chemistry of Archean seafloor hydrothermal vents: Implications for the composition of circa 3.2 Ga seawater. Geochim. Cosmochim. Acta 61, 4025–4042.

Dos Santos, E.C., de Mendonça Silva, J.C., Duarte, H.A., 2016. Pyrite oxidation mechanism by oxygen in aqueous medium. J. Phys. Chem. C. 120, 2760–2768.

Drake, H., Reiners, P.W., 2021. Thermochronological perspectives on the deep-time evolution of the deep biosphere. Proc. Natl. Acad. Sci. U.S.A. 45. e2109609118.

Drake, H., Åström, M.E., Tullborg, E.L., Whitehouse, M., Fallick, A.E., 2013. Variability of sulphur isotope ratios in pyrite and dissolved sulphate in granitoid fractures down to 1 km depth–evidence for widespread activity of sulphur reducing bacteria. Geochim. Cosmochim. Acta 102, 143–161.

Drake, H., Åström, M.E., Heim, C., Broman, C., Åström, J., Whitehouse, M., Ivarsson, M., Siljeström, S., Sjövall, P., 2015. Extreme ^{13}C depletion of carbonates formed during oxidation of biogenic methane in fractured granite. Nat. Commun. 6, 1–9.

Drake, H., Roberts, N.M., Reinhardt, M., Whitehouse, M., Ivarsson, M., Karlsson, A., Kooijman, E., Kielman-Schmitt, M., 2021. Biosignatures of ancient microbial life are present across the igneous crust of the Fennoscandian shield. Commun. Earth Environ. 2, 1–13.

Drennan, G.R., Boiron, M.C., Cathelineau, M., Robb, L.J., 1999. Characteristics of post-depositional fluids in the Witwatersrand Basin. Miner. Petrol. 66, 83–109.

Duane, M.J., Pigozzi, G., Harris, C., 1997. Geochemistry of some deep gold mine waters from the western portion of the Witwatersrand Basin, South Africa. J. African Earth Sci. 24, 105–123.

Edmunds, W.M., Kay, R.L.F., Miles, D.L., Cook, J.M., 1987. The origin of saline groundwaters in the Carnmenellis granite, Cornwall (UK): Further evidence from minor and trace elements. In: Fritz, P., Frape, S.K. (Eds.), Saline Water and Gases in Crystalline Rocks, vol. 33. Geological Association of Canada, Ottawa, ON, pp. 127–143.

Ehlmann, B.L., Mustard, J.F., Murchie, S.L., Bibring, J.P., Meunier, A., Fraeman, A.A., Langevin, Y., 2011. Subsurface water and clay mineral formation during the early history of Mars. Nature 479, 53–60.

Etiope, G., Sherwood Lollar, B., 2013. Abiotic methane on Earth. Rev. Geophys. 51, 276–299.

Farvolden, R.N., Pfannkuch, O., Pearson, R., Fritz, P., 1988. Region 12, Precambrian Shield. In: W., Rosenhein, J.S., Seaber, P.R. (Eds.), The Geology of North America: Hydrogeology Geol. Soc. Am., Boulder, CO., pp. 101–114.

Frape, S.K., Fritz, P., McNut, R.T., 1984. Water-rock interaction and chemistry of groundwaters from the Canadian Shield. Geochim. Cosmochim. Acta 48, 1617–1627.

Frape, S.K., Blyth, A., Stotler, R.L., Ruskeeniemi, T., Blomqvist, R., McNutt, R.H., Gascoyne, M., 2014. 7.15 - Deep Fluids in the Continents. In: Holland, H.D., Turekian, K.K. (Eds.), Treatise on Geochemistry. 2nd ed. Elsevier, Pergamon, pp. 517–562.

Freifeld, B., 2009. The U-tube: a new paradigm for borehole fluid sampling. Sci. Drill. 8, 41–45.

Freifeld, B.M., Trautz, R.C., Kharaka, Y.K., Phelps, T.J., Myer, L.R., Hovorka, S.D., Collins, D.J., 2005. The U-tube: A novel system for acquiring borehole fluid samples from a deep geologic CO_2 sequestration experiment. J. Geophys. Res. 110, B10203.

Frimmel, H.E., 2005. The world's largest gold province: Implications on Archaean atmospheric evolution. In: Mineral Deposit Research: Meeting the Global Challenge. Springer, Berlin, Heidelberg, pp. 949–952.

Frimmel, H.E., 2019. The Witwatersrand Basin and its gold deposits. In: The Archaean Geology of the Kaapvaal Craton, Southern Africa. Springer, Cham, pp. 255–275.

Fritz, P., Frape, S.K., 1982. Saline groundwaters in the Canadian Shield—a first overview. Chem. Geol. 36, 179–190.

Frost, B.R., Beard, J.S., McCaig, A., Condliffe, E., 2008. The formation of micro-rodingites from IODP Hole U1309D: key to understanding the process of serpentinization. J. Petrol. 49, 1579–1588.

Fuchs, S.H., Schumann, D., Williams-Jones, A.E., Murray, A.J., Couillard, M., Lagarec, K., Phaneuf, M.W., Vali, H., 2017. Gold and uranium concentration by interaction of immiscible fluids (hydrothermal and hydrocarbon) in the Carbon Leader Reef, Witwatersrand Supergroup, South Africa. Precambrian Res. 293, 39–55.

Gascoyne, M., Ross, J.D., Purdy, A., Frape, S.K., Drimmie, R.J., 1989. Evidence for penetration of sedimentary basin brines into an Archean granite of the Canadian Shield. In: Miles, D.L. (Ed.), Water-Rock Interaction 6, Malvern, UK. pp. 243–245.

Gold, T., 1992. The deep, hot biosphere. Proc. Natl. Acad. Sci. U.S.A. 89, 6045–6049.

Gray, G.J., Lawrence, S.R., Kenyon, K., Cornford, C., 1998. Nature and origin of 'carbon' in the Archaean Witwatersrand Basin, South Africa. J. Geol. Soc. London 155, 39–59.

Grové, D., Harris, C., 2010. O-and H-isotope study of the Carbon Leader Reef at the Tau Tona and Savuka mines (Western Deep Levels), South Africa: implications for the origin and evolution of Witwatersrand basin fluids. South Afr. J. Geol. 113, 73–86.

Guy, B.M., Ono, S., Gutzmer, J., Kaufman, A.J., Lin, Y., Fogel, M.L., Beukes, N.J., 2012b. A multiple sulfur and organic carbon isotope record from non-conglomeratic sedimentary rocks of the Mesoarchean Witwatersrand Supergroup, South Africa. Precambrian Res. 216, 208–231.

Guy, B.M., Ono, S., Gutzmer, J., Lin, Y., Beukes, N.J., 2014. Sulfur sources of sedimentary "buckshot" pyrite in the auriferous conglomerates of the Mesoarchean Witwatersrand and Ventersdorp Supergroups, Kaapvaal Craton, South Africa. Miner. Depos. 49, 751–775.

Guy, B.M., 2012a. Pyrite in the Mesoarchean Witwatersrand Supergroup, South Africa. Ph.D. Thesis. University of Johannesburg, Johannesburg, South Africa.

Heard, A.W., Warr, O., Borgonie, G., Linage, B., Kuloyo, O., Fellowes, J.W., Magnabosco, C., Lau, M.C., Erasmus, M., Cason, E.D., van Heerden, E., Kieft, T. L., Mabry, J.C., Onstott, T.C., Sherwood Lollar, B., Ballentine, C.J., 2018. South African crustal fracture fluids preserve paleometeoric water signatures for up to tens of millions of years. Chem. Geol. 493, 379–395.

Heath, R.C., 1983. Basic Groundwater Hydrology: US Geological Survey Water Supply Paper 2220; prepared in cooperation with the North Carolina Department of Natural Resources and Community Development.

Hofmann, B.A., 1992. Isolated reduction phenomenon in red beds: A result of porewater radiolysis. In: Kharaka, Y.K., Maest, A.S. (Eds.), Water-Rock Interaction, Rotterdam/Brookfield, pp. 503–506.

Holland, G., Sherwood Lollar, B., Li, L., Lacrampe-Couloume, G., Slater, G.F., Ballentine, C.J., 2013. Deep fracture fluids isolated in the crust since the Precambrian era. Nature 497, 357–360.

Ianni, J.C., 2003. A Comparison of the Bader-Deuflhard and the Cash-Karp Runge-Kutta Integrators for the GRI-MECH 3.0 Model Based on the Chemical Kinetics Code Kintecus. In: Bathe, K.J. (Ed.), Computational Fluid and Solid Mechanics. Elsevier Science Ltd., Oxford, UK, pp. 1368–1372.

Inoue, A., Kurokawa, K., Hatta, T., 2010. Application of chlorite geothermometry to hydrothermal alteration in Toyoha geothermal system, southwestern Hokkaido, Japan. Resour. Geol. 60, 52–70.

Jaguin, J., Boulvais, P., Poujol, M., Boiron, M.C., Cathelineau, M., 2010. Stable isotope composition of quartz-calcite veins in the Witwatersrand basin, South Africa: Implication for basin-scale fluid circulation. South Afr. J. Geol. 113, 169–182.

Kalwasińska, A., Krawiec, A., Deja-Sikora, E., Gołębiewski, M., Kosobucki, P., Swiontek Brzezinska, M., Walczak, M., 2020. Microbial diversity in deep-subsurface hot brines of Northwest Poland: from community structure to isolate characteristics. Appl. Environ. Microbiol. 86, e00252–e00320.

Karolytė, R., Serno, S., Johnson, G., Gilfillan, S.M.V., 2017. The influence of oxygen isotope exchange between CO_2 and H_2O in natural CO_2-rich spring waters: Implications for geothermometry. Appl. Geochem. 84, 173–186.

Karolytė, R., Warr, O., van Heerden, E., Flude, S., de Lange, F., Webb, S., Ballentine, C. J., Lollar, B.S., 2022. The role of porosity in H_2/He production ratios in fracture fluids from the Witwatersrand Basin, South Africa. Chem. Geol. 595, 120788.

Kawabe, I., 1978. Calculation of oxygen isotope fractionation in quartz-water system with special reference to the low temperature fractionation. Geochim. Cosmochim. Acta 42, 613–621.

Kelm, M., Bohnert, E., 2004. A kinetic model for the radiolysis of chloride brine, its sensitivity against model parameters and a comparison with experiments. Forschungszentrum Karlsruhe Wis-senschaftl. Ber., FZKA 6977, Karlsruhe, Germany.

Kharaka, Y.K., Hanor, J.S., 2003. Deep fluids in the continents: I. Sedimentary basins. In: Holland, H.D., Turekian, K.H. (Eds.), Treatise on Geochemistry. Elsevier, Pergamon, pp. 1–48.

Kieft, T.L., McCuddy, S.M., Onstott, T.C., Davidson, M., Lin, L.H., Mislowack, B., Pratt, L., Boice, E., Sherwood, L.B., Lippmann-Pipke, J., Pfiffner, S.M., 2005. Geochemically generated, energy-rich substrates and indigenous microorganisms in deep, ancient groundwater. Geomicrobiol. J. 22, 325–335.

Kieft, T.L., Walters, C.C., Higgins, M.B., Mennito, A.S., Clewett, C.F., Heuer, V., Pullin, M.J., Hendrickson, S., van Heerden, E., Sherwood Lollar, B., Lau, M.C., 2018. Dissolved organic matter compositions in 0.6–3.4 km deep fracture waters, Kaapvaal Craton, South Africa. Org. Geochem. 118, 116–131.

Kiel, S., Glodny, J., Birgel, D., Bulot, L.G., Campbell, K.A., Gaillard, C., Graziano, R., Kaim, A., Lazăr, I., Sandy, M.R., Peckmann, J., 2014. The paleoecology, habitats, and stratigraphic range of the enigmatic Cretaceous brachiopod Peregrinella. PLoS ONE 9, e109260.

Kietäväinen, R., Ahonen, L., Kukkonen, I.T., Hendriksson, N., Nyyssönen, M., Itävaara, M., 2013. Characterisation and isotopic evolution of saline waters of the Outokumpu Deep Drill Hole, Finland-Implications for water origin and deep terrestrial biosphere. J. Appl. Geochem. 32, 37–51.

Kietäväinen, R., Ahonen, L., Kukkonen, I.T., Niedermann, S., Wiersberg, T., 2014. Noble gas residence times of saline waters within crystalline bedrock, Outokumpu Deep Drill Hole, Finland. Geochim. Cosmochim. Acta 145, 159–174.

Kloppmann, W., Girard, J.P., Négrel, P., 2002. Exotic stable isotope compositions of saline waters and brines from the crystalline basement. Chem. Geol. 184, 49–70.

Kovacik Jr., W.P., 2002. Analysis of bacterial transport and survival in the subsurface. Ph.D. Thesis. University of Montana, MT, USA.

Kyle, J.E., Eydal, H.S., Ferris, F.G., Pedersen, K., 2008. Viruses in granitic groundwater from 69 to 450 m depth of the Äspö hard rock laboratory, Sweden. ISME J. 2, 571–574.

Lau, M.C., Cameron, C., Magnabosco, C., Brown, C.T., Schilkey, F., Grim, S., Hendrickson, S., Pullin, M., Sherwood Lollar, B., van Heerden, E., Kieft, T.L., 2014. Phylogeny and phylogeography of functional genes shared among seven terrestrial subsurface metagenomes reveal N-cycling and microbial evolutionary relationships. Front. Microbiol. 5, 531.

Lefticariu, L., Pratt, L.A., LaVerne, J.A., Schimmelmann, A., 2010. Anoxic pyrite oxidation by water radiolysis products—a potential source of biosustaining energy. Earth Planet. Sci. Lett. 292, 57–67.

Li, L., Wing, B.A., Bui, T.H., McDermott, J.M., Slater, G.F., Wei, S., Lacrampe-Couloume, G., Sherwood Lollar, B., 2016. Sulfur mass-independent fractionation in subsurface fracture waters indicates a long-standing sulfur cycle in Precambrian rocks. Nat. Commun. 7, 1–9.

Liang, R., Lau, M.C., Baars, O., Robb, F.T., Onstott, T.C., 2019. Aspartic acid racemization constrains long-term viability and longevity of endospores. FEMS Microbiol. Ecol. 95, fiz132.

Lin, L.H., Hall, J., Lippmann-Pipke, J., Ward, J.A., Sherwood Lollar, B., DeFlaun, M., Rothmel, R., Moser, D., Gihring, T.M., Mislowack, B., Onstott, T.C., 2005a. Radiolytic H_2 in continental crust: nuclear power for deep subsurface microbial communities. Geochem. Geophys. 6, Q07003.

Lin, L.H., Slater, G.F., Sherwood Lollar, B., Lacrampe-Couloume, G., Onstott, T.C., 2005b. The yield and isotopic composition of radiolytic H_2, a potential energy source for the deep subsurface biosphere. Geochim. Cosmochim. Acta 69, 893–903.

Lin, L.H., Wang, P.L., Rumble, D., Lippmann-Pipke, J., Boice, E., Pratt, L.M., Sherwood Lollar, B., Brodie, E.L., Hazen, T.C., Andersen, G.L., DeSantis, T.Z., 2006. Long-term sustainability of a high-energy, low-diversity crustal biome. Science 314, 479–482.

Lippmann-Pipke, J., Stute, M., Torgersen, T., Moser, D.P., Hall, J.A., Lin, L., Borcsik, M., Bellamy, R.E.S., Onstott, T.C., 2003. Dating ultra-deep mine waters with noble gases and ^{36}Cl, Witwatersrand Basin, South Africa. Geochim. Cosmochim. Acta 67, 4597–4619.

Lippmann-Pipke, J., Sherwood Lollar, B., Niedermann, S., Stroncik, N.A., Naumann, R., van Heerden, E., Onstott, T.C., 2011. Neon identifies two billion year old fluid component in Kaapvaal Craton. Chem. Geol. 283, 287–296.

Lollar, G.S., Warr, O., Telling, J., Osburn, M.R., Sherwood Lollar, B., 2019. 'Follow the Water': Hydrogeochemical Constraints on Microbial Investigations 2.4 km Below Surface at the Kidd Creek Deep Fluid and Deep Life Observatory. Geomicrobiol. J. 36, 859–872.

Lovley, D.R., Goodwin, S., 1988. Hydrogen concentrations as an indicator of the predominant terminal electron-accepting reactions in aquatic sediments. Geochim. Cosmochim. Acta 52, 2993–3003.

Lundblad, S., 1994. Evolution of small carbonate platforms in the Umbria-Marche Apennines, Italy. Ph.D. Thesis. University of North Carolina at Chapel Hill, NC, USA.

Magnabosco, C., Ryan, K., Lau, M.C., Kuloyo, O., Sherwood Lollar, B., Kieft, T.L., van Heerden, E., Onstott, T.C., 2016. A metagenomic window into carbon metabolism at 3 km depth in Precambrian continental crust. ISME J. 10, 730–741.

Magnabosco, C., Lin, L.H., Dong, H., Bomberg, M., Ghiorse, W., Stan-Lotter, H., Pedersen, K., Kieft, T.L., van Heerden, E., Onstott, T.C., 2018. The biomass and biodiversity of the continental subsurface. Nat. Geosci. 11, 707–717.

Maréchal, J.C., Sarma, M.P., Ahmed, S., Lachassagne, P., 2002. Establishment of earth tide effect on water-level fluctuations in an unconfined hard rock aquifer using spectral analysis. Curr. Sci. 83, 61–64.

Martineau, F., Fourel, F., Bodergat, A.M., Lécuyer, C., 2012. D/H equilibrium fractionation between H_2O and H_2 as a function of the salinity of aqueous solutions. Chem. Geol. 291, 236–240.

McArthur, J.M., Rio, D., Massari, F., Castradori, D., Bailey, T.R., Thirlwall, M., Houghton, S., 2006. A revised pliocene record for marine-$^{87}Sr/^{86}Sr$ used to date an interglacial event recorded in the Cockburn Island Formation, Antarctic Peninsula. Palaeogeogr. Palaeoclimatol. Palaeoecol. 242, 126–136.

McKay, C.P., Anbar, A.D., Porco, C., Tsou, P., 2014. Follow the plume: the habitability of Enceladus. Astrobiology 14, 352–355.

McNutt, R.H., 2000. Strontium isotopes. Environmental tracers in subsurface hydrology. In: Cook, P.G., Herczeg, A.L. (Eds.), Springer, Boston, MA, pp. 233–260.

McNutt, R.H., Frape, S.K., Fritz, P., Jones, M.G., MacDonald, I.M., 1990. The $^{87}Sr/^{86}Sr$ values of Canadian Shield brines and fracture minerals with applications to groundwater mixing, fracture history, and geochronology. Geochim. Cosmochim. Acta 54, 205–215.

Mngadi, S.B., Durrheim, R.J., Manzi, M.S.D., Ogasawara, H., Yabe, Y., Yilmaz, H., Wechsler, N., Van Aswegen, G., Roberts, D., Ward, A.K., Naoi, M., 2019. Integration of underground mapping, petrology, and high-resolution microseismicity analysis to characterise weak geotechnical zones in deep South African gold mines. Int. J. Rock Mech. Min. Sci. 114, 79–91.

Mokadem, F., Parkinson, I.J., Hathorne, E.C., Anand, P., Allen, J.T., Burton, K.W., 2015. High-precision radiogenic strontium isotope measurements of the modern and

glacial ocean: Limits on glacial–interglacial variations in continental weathering. Earth Planet. Sci. Lett. 415, 111–120.

Möller, P., Weise, S.M., Althaus, E., Bach, W., Behr, H.J., Borchardt, R., Bräuer, K., Drescher, J., Erzinger, J., Faber, E., Hansen, B.T., 1997. Paleofluids and recent fluids in the upper continental crust: Results from the German Continental Deep Drilling Program (KTB). J. Geophys. Res. Solid Earth 102, 18233–18254.

Nebel, O., Scherer, E.E., Mezger, K., 2011. Evaluation of the ^{87}Rb decay constant by age comparison against the U-Pb system. Earth Planet. Sci. Lett. 301, 1–8.

Nkosi, Z.N., Manzi, M.S.D., Westgate, M., Roberts, D., Durrheim, R.J., Ogasawara, H., 2022. Physical property studies to elucidate the source of seismic reflectivity within the ICDP DSeis seismogenic zone: Klerksdorp goldfield, South Africa. Int. J. Rock Mech. Min. Sci. 155, 105082.

Nordstrom, D.K., Olsson, T., Carlsson, L., Fritz, P., 1989. Introduction to the hydrogeochemical investigations within the International Stripa Project. Geochim. Cosmochim. Acta 53, 1717–1726.

Nuppunen-Puputti, M., Purkamo, L., Kietäväinen, R., Nyyssönen, M., Itävaara, M., Ahonen, L., Kukkonen, I., Bomberg, M., 2018. Rare biosphere archaea assimilate acetate in Precambrian terrestrial subsurface at 2.2 km depth. Geosciences 8, 418.

Omar, G.I., Onstott, T.C., Hoek, J., 2003. The origin of deep subsurface microbial communities in the Witwatersrand Basin, South Africa as deduced from apatite fission track analyses. Geofluids 3, 69–80.

O'Neil, J.R., Clayton, R.N., Mayeda, T.K., 1969. Oxygen isotope fractionation in divalent metal carbonates. J. Chem. Phys. 51, 5547–5558.

Onstott, T.C., Lin, L.H., Davidson, M., Mislowack, B., Borcsik, M., Hall, J., Slater, G., Ward, J., Sherwood Lollar, B., Lippmann-Pipke, J., Boice, E., 2006. The origin and age of biogeochemical trends in deep fracture water of the Witwatersrand Basin, South Africa. Geomicrobiol. J. 23, 369–414.

Payler, S.J., Biddle, J.F., Sherwood Lollar, B., Fox-Powell, M.G., Edwards, T., Ngwenya, B.T., Paling, S.M., Cockell, C.S., 2019. An ionic limit to life in the deep subsurface. Front. Microbiol. 10, 426.

Pearson Jr., F.J., 1987. Models of mineral controls on the composition of saline groundwaters of the Canadian Shield. In: Fritz, P., Frape, S.K. (Eds.), Saline Water and Gases in Crystalline Rocks, Geological Association of Canada (Special Paper), pp. 39–51.

Pester, N.J., Conrad, M.E., Knauss, K.G., DePaolo, D.J., 2018. Kinetics of D/H isotope fractionation between molecular hydrogen and water. Geochim. Cosmochim. Acta 242, 191–212.

Peucker-Ehrenbrink, B., Fiske, G.J., 2019. A continental perspective of the seawater ^{87}Sr/^{86}Sr record: a review. Chem. Geol. 510, 140–165.

Pfiffner, S.M., Cantu, J.M., Smithgall, A., Peacock, A.D., White, D.C., Moser, D.P., Onstott, T.C., van Heerden, E., 2006. Deep subsurface microbial biomass and community structure in Witwatersrand Basin mines. Geomicrobiol. J. 23, 431–442.

Philippot, P., Van Zuilen, M., Lepot, K., Thomazo, C., Farquhar, J., Van Kranendonk, M. J., 2007. Early Archaean microorganisms preferred elemental sulfur, not sulfate. Science 317, 1534–1537.

Pienaar, D., Guy, B.M., Hofmann, A., Viljoen, K.S., 2015. A geometallurgical characterization of the Vaal Reef A-facies at the Moab Khotsong mine, Klerksdorp Goldfield, South Africa. South Afr. J. Geol. 118, 455–472.

Pope, E.C., Bird, D.K., Rosing, M.T., 2012. Isotope composition and volume of Earth's early oceans. Proc. Natl. Acad. Sci. U.S.A. 109, 4371–4376.

Powell, J.L., 1962. The strontium isotopic composition and origin of carbonatites. Ph. D. Thesis. Massachusetts Institute of Technology, MA, USA.

Purkamo, L., Bomberg, M., Kietäväinen, R., Salavirta, H., Nyyssönen, M., Nuppunen-Puputti, M., Ahonen, L., Kukkonen, I., Itävaara, M., 2016. Microbial co-occurrence patterns in deep Precambrian bedrock fracture fluids. Biogeosciences 13, 3091–3108.

Purtschert, R., Yokochi, R., Jiang, W., Lu, Z.T., Mueller, P., Zappala, J., van Heerden, E., Cason, E., Lau, M., Kieft, T.L., Gerber, C., 2021. Underground production of ^{81}Kr detected in subsurface fluids. Geochim. Cosmochim. Acta 295, 65–79.

Robb, L.J., Robb, V.M., 1998. Gold in the Witwatersrand basin. In: The Mineral Resources of South Africa, Handbook. Council for Geosciences (CGS), Pretoria, pp. 294–349.

Schrenk, M.O., Brazelton, W.J., Lang, S.Q., 2013. Serpentinization, carbon, and deep life. Rev. Mineral. Geochem. 75, 575–606.

Sherwood Lollar, B., Westgate, T.D., Ward, J.A., Slater, G.F., Lacrampe-Couloume, G., 2002. Abiogenic formation of alkanes in the Earth's crust as a minor source for global hydrocarbon reservoirs. Nature 416, 522–524.

Sherwood Lollar, B., Lacrampe-Couloume, G., Slater, G.F., Ward, J., Moser, D.P., Gihring, T.M., Lin, L.H., Onstott, T.C., 2006. Unravelling abiogenic and biogenic sources of methane in the Earth's deep subsurface. Chem. Geol. 226, 328–339.

Sherwood Lollar, B., Lacrampe-Couloume, G., Voglesonger, K., Onstott, T.C., Pratt, L. M., Slater, G.F., 2008. Isotopic signatures of CH_4 and higher hydrocarbon gases from Precambrian Shield sites: a model for abiogenic polymerization of hydrocarbons. Geochim. Cosmochim. Acta 72, 4778–4795.

Sherwood Lollar, B., Onstott, T.C., Lacrampe-Couloume, G., Ballentine, C.J., 2014. The contribution of the Precambrian continental lithosphere to global H_2 production. Nature 516, 379–382.

Sherwood Lollar, B., Heuer, V.B., McDermott, J., Tille, S., Warr, O., Moran, J.J., Telling, J., Hinrichs, K.U., 2021. A window into the abiotic carbon cycle–Acetate and formate in fracture waters in 2.7 billion year-old host rocks of the Canadian Shield. Geochim. Cosmochim. Acta 294, 295–314.

Shin, H.S., Kim, Y.R., Ponomarev, A.V., 2001. Influence of sulfite on radiolytic conversion of nitrate and nitrite in dilute aqueous solutions. Mendeleev Commun. 11, 21–23.

Shouakar-Stash, O., Alexeev, S.V., Frape, S.K., Alexeeva, L.P., Drimmie, R.J., 2007. Geochemistry and stable isotopic signatures, including chlorine and bromine isotopes, of the deep groundwaters of the Siberian Platform, Russia. Appl. Geochem. 22, 589–605.

Silver, B.J., Raymond, R., Sigman, D., Prokopenko, M., Sherwood Lollar, B., Lacrampe-Couloume, G., Fogel, M., Pratt, L., Lefticariu, L., Onstott, T.C., 2012. The origin of NO_3 and N_2 in deep subsurface fracture water of South Africa. Chem. Geol. 294, 51–62.

Simkus, D.N., Slater, G.F., Sherwood Lollar, B., Wilkie, K., Kieft, T.L., Magnabosco, C., Lau, M.C., Pullin, M.J., Hendrickson, S.B., Wommack, K.E., Sakowski, E.G., 2016. Variations in microbial carbon sources and cycling in the deep continental subsurface. Geochim. Cosmochim. Acta 173, 264–283.

Stober, I., Bucher, K., 2007. Hydraulic properties of the crystalline basement. Hydrogeol. J. 15, 213–224.

Stotler, R.L., Frape, S.K., Ruskeeniemi, T., Ahonen, L., Onstott, T.C., Hobbs, M.Y., 2009. Hydrogeochemistry of groundwaters in and below the base of thick permafrost at Lupin, Nunavut, Canada. J. Hydrol. 373, 80–95.

Stotler, R.L., Frape, S.K., Shouakar-Stash, O., 2010. An isotopic survey of δ^{81}Br and δ^{37}Cl of dissolved halides in the Canadian and Fennoscandian Shields. Chem. Geol. 274, 38–55.

Strickland, J.D.H., Parsons, T.R., 1972. A practical handbook of seawater analysis, 2nd edition – Bulletin 167, in: Cook, D.G., Reinhart, J.M., Stevenson, J.C., Watson, J. (Eds.), Fisheries Research Board of Canada, Ottowa, pp. 87–89.

Tarnas, J.D., Mustard, J.F., Sherwood Lollar, B., Stamenković, V., Cannon, K.M., Lorand, J.P., Onstott, T.C., Michalski, J.R., Warr, O., Palumbo, A.M., Plesa, A.C., 2021. Earth-like habitable environments in the subsurface of Mars. Astrobiology 21, 741–756.

Tucker, R.F., Viljoen, R.P., Viljoen, M.J., 2016. A Review of the Witwatersrand Basin-The World's greatest goldfield. Episodes 39, 105–133.

Tuffour, H.O., IBY, M.B., Adjei-Gyapong, T., Khalid, A.A., Abubakar, A., Melenya, C., Kpotor, P., 2014. Soil organic carbon: relating the Walkley-Black wet oxidation method to loss on ignition and clay content. Int. J. Sci. Knowl. 2, 249–256.

Veizer, J., Compston, W., 1976. ^{87}Sr/^{86}Sr in Precambrian carbonates as an index of crustal evolution. Geochim. Cosmochim. Acta 40, 905–914.

Veizer, J., Hoefs, J., Ridler, R.H., Jensen, L.S., Lowe, D.R., 1989. Geochemistry of Precambrian carbonates: I. Archean hydrothermal systems. Geochim. Cosmochim. Acta 53, 845–857.

Vosloo, J.C., 2008. A new minimum cost model for water reticulation systems on deep mines. Ph.D. Thesis. North-West Univ., Potchefstroom, South Africa.

Vovk, I.F., 1981. Radiolytic model of formation brine composition in the crystalline basement of shields. Geokhimiya 4, 467–480.

Vovk, I.F., 1982. Saline Brines in Crystalline Basement Rocks. Ukrainian Academy of Science, Kiev, p. 163.

Vovk, I.F., 1987. Radiolytic salt enrichment and brines in the crystalline basement of the East European Platform. In: Fritz, P., Frape, S.K. (Eds.), Saline Waters and Gases in Crystalline Rocks GAC Special Paper 33, pp. 197–210.

Ward, J.A., Slater, G.F., Moser, D.P., Lin, L.H., Lacrampe-Couloume, G., Bonin, A.S., Davidson, M., Hall, J.A., Mislowack, B., Bellamy, R.E.S., Onstott, T.C., Sherwood Lollar, B., 2004. Microbial hydrocarbon gases in the Witwatersrand Basin, South Africa: implications for the deep biosphere. Geochim. Cosmochim. Acta 68, 3239–3250.

Warr, O., Sherwood Lollar, B., Fellowes, J., Sutcliffe, C.N., McDermott, J.M., Holland, G., Mabry, J.C., Ballentine, C.J., 2018. Tracing ancient hydrogeological fracture network age and compartmentalization using noble gases. Geochim. Cosmochim. Acta 222, 340–362.

Warr, O., Giunta, T., Ballentine, C.J., Sherwood Lollar, B., 2019. Mechanisms and rates of ^{4}He, ^{40}Ar, and H_2 production and accumulation in fracture fluids in Precambrian Shield environments. Chem. Geol. 530, 119322.

Warr, O., Giunta, T., Onstott, T.C., Kieft, T.L., Harris, R.L., Nisson, D.M., Sherwood Lollar, B., 2021. The role of low-temperature ^{18}O exchange in the isotopic evolution of deep subsurface fluids. Chem. Geol. 561, 120027.

Warr, O., Ballentine, C.J., Onstott, T.C., Nisson, D.M., Kieft, T.L., Hillegonds, D.J., Sherwood Lollar, B., 2022. Novel ^{86}Kr excess and other noble gases identify a billion-year-old radiogenically-enriched groundwater system. Nat. Comms. 13, 3768.

Whitehouse, M.J., 2013. Multiple Sulfur Isotope Determination by SIMS: Evaluation of Reference Sulfides for Δ^{33}S with Observations and a Case Study on the Determination of Δ^{36}S. Geostand. Geoanal. Res. 37, 19–33.

Wilson, A.H., Zeh, A., Gerdes, A., 2017. In situ Sr isotopes in plagioclase and trace element systematics in the lowest part of the eastern Bushveld Complex: dynamic processes in an evolving magma chamber. J. Petrol. 58, 327–360.

Worden, R.H., Griffiths, J., Wooldridge, L.J., Utley, J.E.P., Lawan, A.Y., Muhammed, D. D., Simon, N., Armitage, P.J., 2020. Chlorite in sandstones. Earth Sci. Rev. 204, 103105.

Worman, S.L., Pratson, L.F., Karson, J.A., Klein, E.M., 2016. Global rate and distribution of H_2 gas produced by serpentinization within oceanic lithosphere. Geophys. Res. Lett. 43, 6435–6443.

Young, E.D., Kohl, I.E., Sherwood Lollar, B., Etiope, G., Rumble Iii, D., Li, S., Haghnegahdar, M.A., Schauble, E.A., McCain, K.A., Foustoukos, D.I., Sutclife, C., 2017. The relative abundances of resolved $^{12}CH_2D_2$ and $^{13}CH_3D$ and mechanisms controlling isotopic bond ordering in abiotic and biotic methane gases. Geochim. Cosmochim. Acta 203, 235–264.

Zhao, B., Robb, L.J., Harris, C., Jordaan, L., 2006. Origin of hydrothermal fluids and gold mineralization associated with the Ventersdorp Contact Reef, Witwatersrand basin, South Africa: Constraints from S, O, and H isotopes (Special Paper). Geol. Soc. Am. 405, 333–352.